Zainal *et al. Int J Concr Struct Mater (2021) 15:20*
https://doi.org/10.1186/s40069-021-00457-w

International Journal of Concrete Structures and Materials

RESEARCH

Open Access

Enhancing the Performance of Knee Beam–Column Joint Using Hybrid Fibers Reinforced Concrete

S. M. Iqbal S. Zainal, Farzad Hejazi* and Raizal S. M. Rashid

Abstract

The knee beam–column joint is a critical location in a Reinforced Concrete (RC) structure particularly when subjected to earthquake vibrations. The current structural design codes dictate the use of high amounts of steel reinforcements in the frame joint to manage large strain demands in seismic-prone regions. However, these codes could result in the congestion of steel reinforcements in the limited joint area which can consequently produce numerous construction complications. This study aims to improve the structural performance of Knee Joint (KJ) by reducing the load induced to the embedded steel reinforcements during seismic vibrations. Hence, this study attempted to develop a Hybrid Fiber Reinforced Concrete (HyFRC) by combining multiple synthetic fibers to be introduced onto KJ. Six KJ specimens were cast using five developed HyFRC materials and one Control specimen to be experimentally tested under lateral cyclic loading. The results indicated significant improvements for the HyFRC KJ specimens particularly in energy dissipation capacity, stiffness degradation rate, displacement ductility toughness, steel reinforcement strain and hysteretic behavior. A total of six Finite Element (FE) KJ models were developed using the HyFRC materials to verify the results from the experimental testing. The accuracy of the proposed FE models resulted in average percentage differences of 25.89% for peak load, 3.45% for peak load displacement and 0.18% for maximum displacements from the experimental data. In conclusion, this study developed HyFRC materials that are beneficial in providing cost-efficient alternatives to Reinforced Concrete (RC) KJ structures in areas with low to moderate level of seismic risks.

Keywords: FORTA Fibers, Synthetic Fibers, Hybrid Fiber Reinforced Concrete, Fiber Reinforced Concrete, Knee Joint, Beam–Column, Toughness, Cyclic Loading

1 Introduction

Tremors caused by unpredictable and violent earthquakes can inflict significant damage towards the Reinforced Concrete (RC) structures. Therefore, it is important to reinforce structures in seismic-prone regions to limit structural damages and prevent a total collapse of structures. Having said that, the beam–column joint is one of the critical points within a structure that is susceptible to excessive damage during earthquakes (Bindhu et al. 2009; Chun and Shin 2014). In an RC framed structure, forces from columns and adjacent beams are transferred through the beam–column joints. When subjected to the combined accumulation of compressive, tensile and shear forces, these joints succumb to the highest damages during earthquakes. Therefore, strengthening these joints could increase the structural ductility to resist more deformation before the connection fails (Parastesh et al. 2014).

To retain the strength and stiffness of the joint area, current design loads require a higher amount of transverse reinforcements in the column encompassing the joint (Joint ACI-ASCE Committee 2002; NA to BS EN 2008). However, increasing steel reinforcements has

*Correspondence: farzad@fhejazi.com
Department of Civil Engineering, Universiti Putra Malaysia, 43400 Putra, Selangor, Malaysia
Journal information: ISSN 1976-0485 / eISSN 2234-1315

caused several problems during construction. One of the evident problems is the limited available space in the beam–column joint, whereby having a high percentage of steel reinforcements would contribute to steel congestions. These congestions, in turn, will lead to on-site complications including wet concrete not being able to be compacted properly, resulting in steel reinforcements end up partially covered by wet concrete. This condition could cause steel corrosion, thus weakening the performance of steel reinforcements by producing hollow space and cavities inside the concrete known as honeycombs which could lead to bond-slip failure of the primary reinforcements (Foroughi-Asl et al. 2008; Kang et al. 2010).

The current technologies which can solve the steel congestion problems include Self-Compacting Concrete (SCC), fibrous cementitious composites and headed deformed bars. However, the SCC and headed deformed bar require experts to supervise the concrete mix and installation as it is complex to be carried out (Nakaki et al. 2014). Meanwhile, the incorporation of Fiber Reinforced Concrete (FRC) minimizes large strain deformations in steel due to the applied stresses, which can lead to decreased quantity of steel reinforcement in the joint (Altoubat et al. 2009; Khanlou et al. 2012). It is also more straightforward, quick and economical as it does not require specialized labor and, hence, is more practical on-site.

However, the use of single fiber in FRC could limit the fiber-bridging capabilities because they are bounded by crack zones and volume fraction limitations (Fu et al. 2018; Guler 2018). Cracking is a multiscale and gradual process, where microcracks coalesce into macro-cracks which propagate at a stable rate until instability occurs and fractures the cementitious composites. Moreover, the use of only one type of fiber implies that it would only be able to reinforce one level of crack within its cracking-strain limit (Swolfs et al. 2014; Yao 2019). Hence, high-volume fractions of fibers were typically designed to overcome the strain limit, but caused workability complications during concrete casting (Siva Chidambaram and Agarwal 2018). The hybridization of two or more different types of fibers in a cement matrix like the Hybrid Fiber Reinforced Concrete (HyFRC) can reinforce a higher range of crack levels (Nayar and Gettu 2015), reduce applied damage (Sahoo et al. 2014) and achieve equal or greater performance capability than that of the single-FRC (Soutsos et al. 2012). Several HyFRC are more effective than the traditional FRC in bridging micro-crack as they result in strain-hardening of concrete and improve post-cracking mode of failure (Yap et al. 2014).

Fibers are usually hybridized between a primary load-bearing fiber and a secondary fiber. Steel fibers are widely popular as the load-bearing fiber in any combination mix due to its high strength (Mo et al. 2017), stiffness (Thomas and Ramaswamy 2007), ductility (Wille and Naaman 2012) and large macro-size compared to the other types of fiber. However, recent developments in producing macro-synthetic fibers might break the over-dependency on steel fibers as the primary choice for the load-bearing fiber (McCraven 2002). Macro-sized synthetic fibers are more advantageous as they are more economical than steel fibers and can achieve similar reinforcing capabilities (Buratti et al. 2011; Yin et al. 2015), produce significantly lower carbon footprint (Shen et al. 2010; Strezov and Herbertson 2006), and are non-corrosive compared to steel, which is known to deteriorate in performance over time. The use of more than 2% steel fibers in concrete can also lead to fiber segregation and air entrapment which could affect the tensile and flexural stress-resisting capabilities of the fibers (Chidambaram and Agarwal 2015).

The strengthening of the beam–column joint using FRC depends on the capacity of fibers inside the concrete to retain excessive loads and reduce damages on steel reinforcement connections. Although the mechanical properties of FRC in compression, flexure, tension, and shear can be determined from experimental tests, the results should not be used as a basis for the material to be applied universally on all structural components, particularly for the beam–column joints. It is because the performance of the beam–column joint differs with different structural configurations. Desired results of using steel FRC in external beam–column joints should not be fundamentally translated to improved performance in the external, T or knee beam–column joints. Moreover, the knee-type beam–column arrangement was identified to be the weakest among the interior, exterior and T-type connections (Xue and Yang 2014). The absence of lateral and vertical restraints due to its discontinuous L-shaped assembly resulted in an unbalanced structure. Therefore, the knee-type connection is susceptible to more damages compared to the other joints during seismic vibrations and might require tougher FRC joints.

The proposed solutions to address the known failure modes of Knee Joints (KJ) include using higher steel reinforcement ratios and increasing the size of steel reinforcements to contain the diagonal tension crack and splitting crack failure on the joint section. However, previous studies revealed that the proposed solutions caused heavy congestion of steel in the joint, making it difficult to arrange the reinforcement based on specific ductile detailing, compacting concrete and providing adequate anchoring of reinforcements (Kheni et al. 2015; Parastesh et al. 2014). Furthermore, satisfying the minimum design requirement does not guarantee life safety and prevention of structural failure

(Hossein and Shariatmadar 2018). Thus, it was deduced that the beam–column connection remains the weakest link even if designed using current model building codes due to the critical confinement hinge region which limits the placement of steel reinforcements (Khose et al. 2012; Tsonos 2007).

Therefore, in this study, multiple fibers were hybridized in the cement matrix to overcome the limitation of single-fiber concrete. These HyFRC can reinforce a higher range of crack levels, reduce applied damage and achieve equal or greater performance capability than the single-FRC. These HyFRC could prevent steel congestion on the joint section by reducing damage applied to steel reinforcements while also improving the performance of KJ under reversed cyclic loading.

2 Proposed Synthetic Hybrid Fiber Reinforced Concrete

This study hybridized synthetic fibers manufactured by FORTA Corporation (Grove City, PA, USA) with varying parameters such as tensile strength, length, diameter, bonding power, fiber volume fraction, material and fiber form. The Ferro macro-synthetic fibers which were selected as the primary load-bearing fiber in this hybridization were used in dual lengths to maximize performance (Akkaya et al. 2006). The secondary fibers in the proposed hybrids included the Ultra-Net, Super-Net,

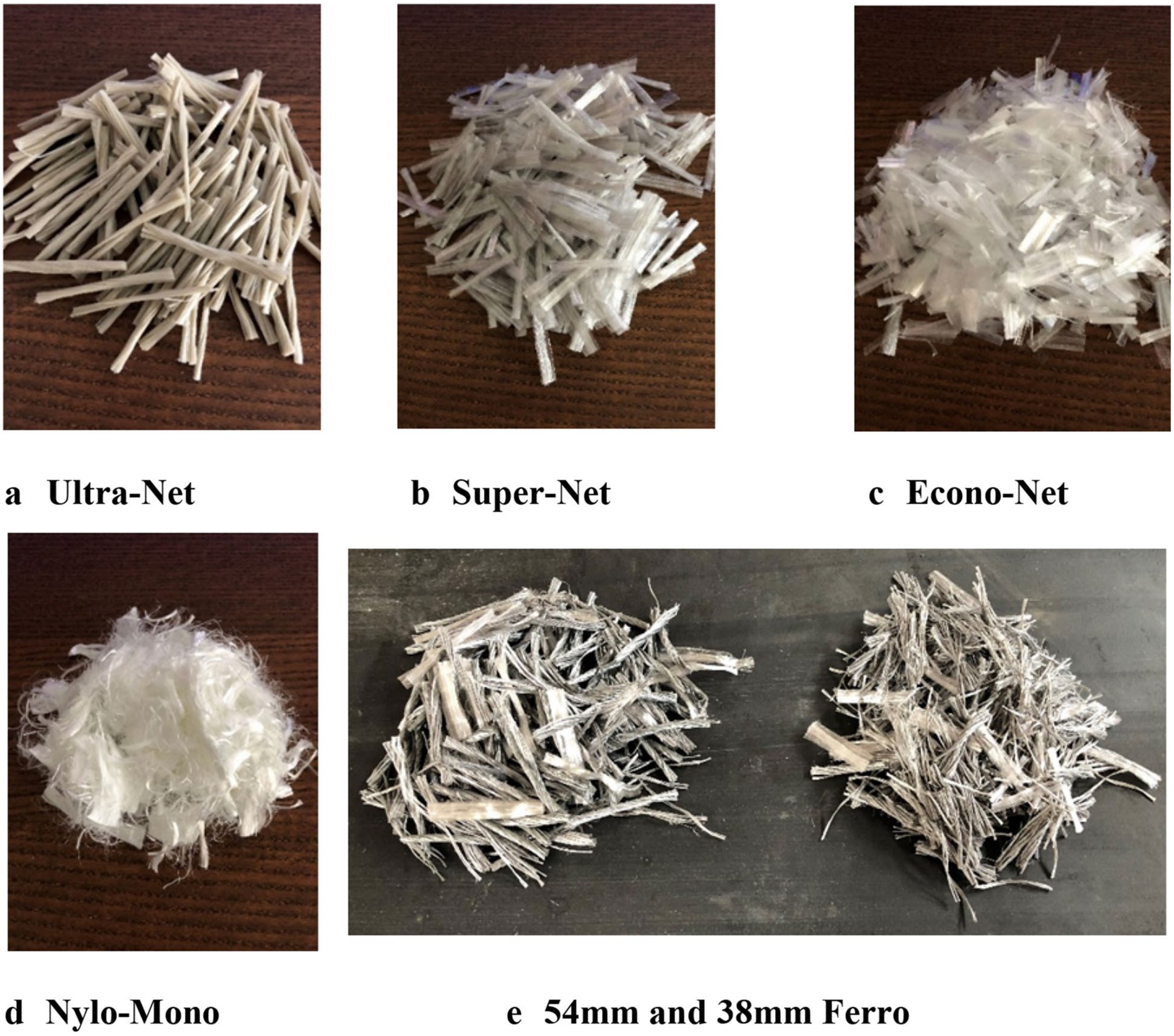

Fig. 1 FORTA micro- and macro-fibers

Table 1 FORTA fibers technical data (UN: Ultra-Net, SN: Super-Net, EN: Econo-Net, NM: Nylo-Mono, FF: Ferro)

Type	Length (mm)	Form	Bonding Power	Class	Material	Tensile Strength (MPa)
UN	54	Fibrillated Twisted Bundle	Extra heavy-duty	Micro	Polypropylenea and Additives	570–660
SN	38	Fibrillated	Heavy-duty			570–660
EN	38	Fibrillated	Medium-duty			570–660
NM	19	Monofilament	Light-duty		Virgin Nylon	966
FF1	38	Fibrillated Twisted Bundle	Heavy-duty	Macro	Polyethylene, Polypropyleneaand Additives	1100
FF2	54		Heavy-duty			570–660

Econo-Net and Nylo-Mono micro-class fibers. Figure 1 illustrates all the fibers used in fiber hybridization. Table 1 summarizes the fiber properties.

This study is a continuation of a 4-part research conducted on fiber hybridization (Zainal et al. 2020a, 2020b). In this study, a total of five hybrid combinations were designed with one plain concrete as the control. Table 2 lists all the hybrid mixes designed in this study. The two levels of volume fractions devised for the Ferro fibers were 0.4% and 0.6%. The remaining microfibers were hybridized in the range of 0.2% and 0.3%. The fiber dosages were based on the mass of cement content used.

The concrete used in this study is designed based on Teychenne Building Research Establishment (BRE) design of normal concrete mixes (Teychenne et al. 1997). The materials used include cement = 409 kg/m^3; water = 225 kg/m^3; sand = 836 kg/m^3; 10 mm coarse aggregates = 302 kg/m^3; 20 mm coarse aggregates = 604 kg/m^3. Meanwhile, Portland cement Type II was used from various sources. All of the specimens were cured for 28 days under a wet burlap before testing.

3 Details of knee beam–column joint

The knee beam–column connection design considered in this study is based on a previous study from the University of Toronto (Angelakos 1999). It represents a half-scale KJ of a twenty-story moment-resisting frame structure in an area of high seismic risk. All of the specimens were cast at the structural laboratory of Universiti Putra Malaysia (UPM) and moist-cured with wet burlap wrapping for 28 days before testing. The beam–column section was cast with plain concrete followed by the HyFRC materials on the joint section 24 h later. A total of six knee beam–column joints were prepared with five HyFRC and one plain concrete specimen. The HyFRC joint region was cast using the Ferro-Ultra (F6U3), Ferro-Super (F6S3), Ferro-Econo (F6E3) and Ferro-Nylo (F6N3) hybrid-mix design as indicated in Fig. 2.

The test specimen is primarily divided into three major components, the column, joint and beam. The joint is the intersection area between the column and beam. In this study, the joint was extended 250 mm horizontally to the beam and 250 mm vertically to the column from the cube core joint. This joint area was cast using the developed HyFRC materials while the other structural parts used plain concrete, as recommended in section A.1 in the ACI building code (ACI Committee 374 2002). Details of the specimens are displayed in Fig. 3.

The main reinforcing steel reinforcements for both the beam and column were terminated at the joint with a 90° hook, and an 80 mm stirrup and hoop spacing, as illustrated in Fig. 4. Four stirrups and four hoops were positioned at the joint core (400 × 400 × 400 mm). All reinforcements have a 20 mm concrete cover from the

Table 2 Proposed HyFRC for Beam–Column joint (C: Control; UN: Ultra-Net; SN: Super-Net; EN: Econo-Net; FF: Ferro)

Specimens	Designation	Type of Fibers (Vol. of Fraction, %)						Total Vol. Fraction, %
		Macrofibers		Microfibers				
		FF1	FF2	UN	SN	EN	NM	
1	Control	-	-	-	-	-	-	-
2	FFC	0.6	0.6	-	-	-	-	1.20
3	F6U3	0.6	0.6	0.30	-	-	-	1.50
4	F6S3	0.6	0.6	-	0.30	-	-	1.50
5	F6E3	0.6	0.6	-	-	0.30	-	1.50
6	F6N3	0.6	0.6	-	-	-	0.30	1.50

Fig. 2 The **a** casting of plain concrete on beam–column sections, **b** concrete compaction and fresh concrete inside the beam–column molding, **c** strain gages installed on the steel reinforcements and **d** the moist-curing of the HyFRC specimens using wet burlap

embedded steel to the external surface. Additionally, the reinforcement specifications and the average compressive strengths for all specimens are listed in Table 3. The compressive strengths were determined from eighteen 150 × 300 mm concrete cylinders using the Standard Test Method for Compressive Strength of Cylindrical Concrete Specimens (ASTM C39/C39M-16a 2016). All the cylinders were cured using wet burlap for 28 days to simulate the curing undergone by the half-scale KJ specimens.

4 Experimental test procedure

A dynamic Actuator with 300 kN load capacity was used to impose quasi-static lateral cyclic loading on the knee beam–column specimens. The tests were displacement controlled using the load history based on the ACI code (ACI Committee 374 2002) illustrated in Fig. 5. Three full cycles were completed for each increment in amplitude. The maximum displacement was defined at 100 mm with three cycles for every increment in amplitude.

The experimental testing was set-up according to previous tests with certain adjustments made to conform to the structural laboratory in Universiti Putra Malaysia. The conceptional layout of the experimental set-up

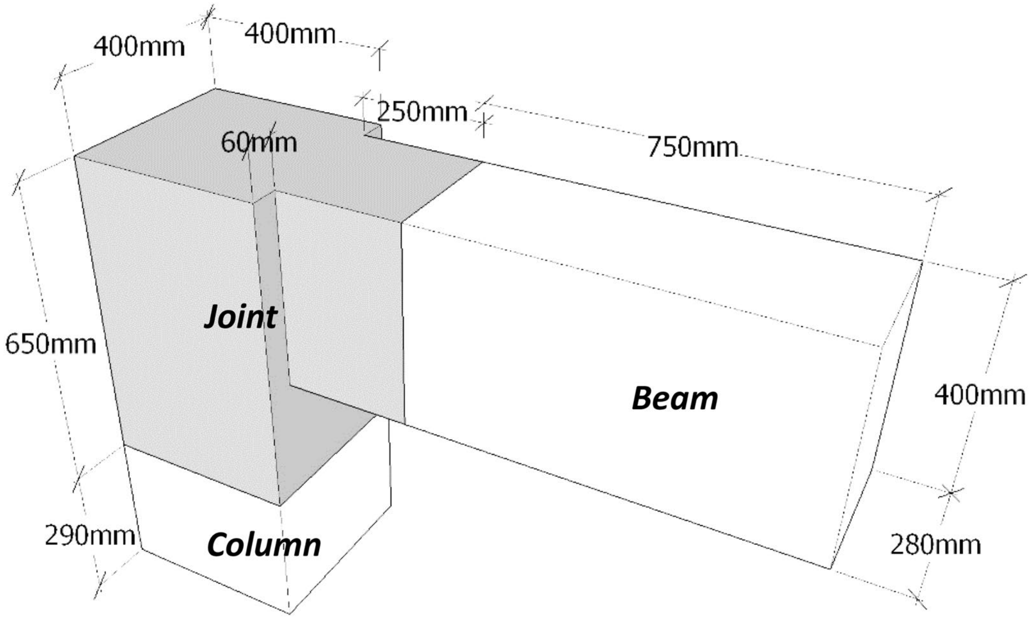

Fig. 3 Specimen Geometric Details with shaded regions as the HyFRC

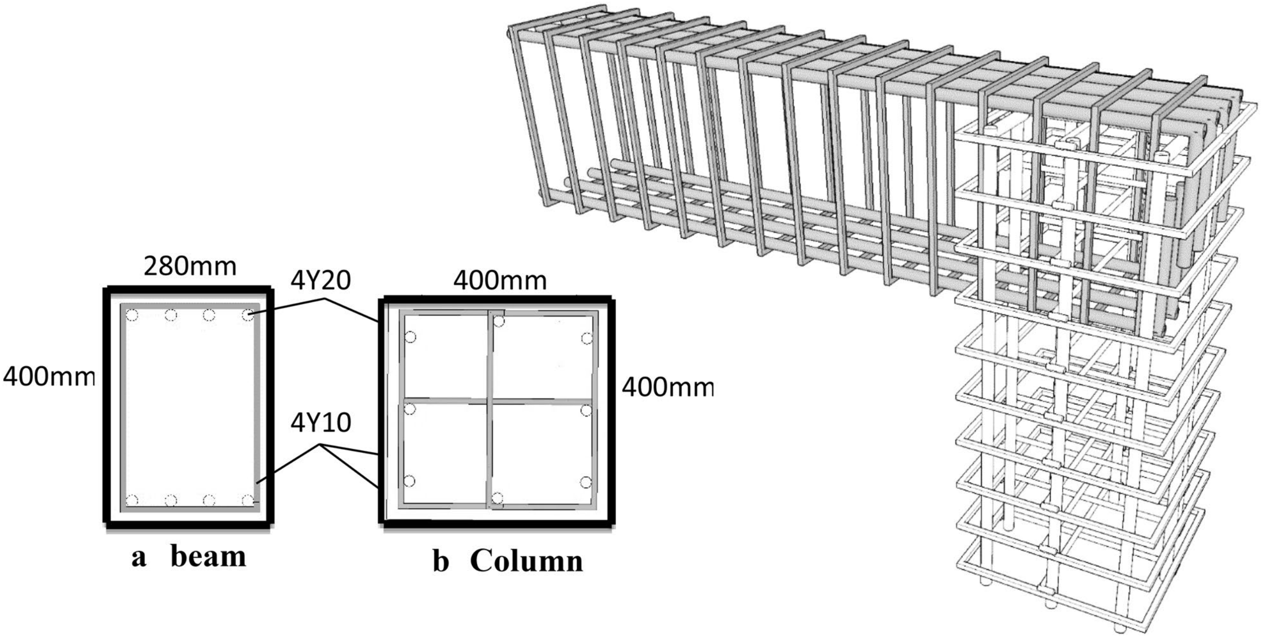

Fig. 4 Steel reinforcements layout with reinforcement cross section

is depicted in Fig. 6. The base of the column was seated to an elevated extension fixed to the strong floor, while the vertical HSS member was pinned to the jig connecting the beam to the actuator. The seating prevents lateral movement but only allows rotation in the pushing and pulling directions.

Also, a dynamic Linear Variable Displacement Transducers (LVDT) was placed at the back of the joint using a vertical support system to measure the push–pull action of the beam–column specimens as presented in Fig. 7. Two 5 mm steel strain gauges were installed on the stirrups at the joint, near the beam–column interfacial

Table 3 Steel reinforcement details

No.	Concrete in ntmolumns	Concrete in joint section	Concrete compressive strength for joints section (MPa)	Steel Yield Strength (MPa)	Column Reinforcement	Beam Reinforcement (Top and Bottom)	Shear Reinforcements	
							Hoops	Stirrups
1	C (Plain)	C (Plain)	25.53	500	4Y20	4Y20	4Y10	4Y10
2	C (Plain)	FFC	31.60	500	4Y20	4Y20	4Y10	4Y10
3	C (Plain)	F6U3	27.00	500	4Y20	4Y20	4Y10	4Y10
4	C (Plain)	F6S3	23.89	500	4Y20	4Y20	4Y10	4Y10
5	C (Plain)	F6E3	26.91	500	4Y20	4Y20	4Y10	4Y10
6	C (Plain)	F6N3	25.57	500	4Y20	4Y20	4Y10	4Y10

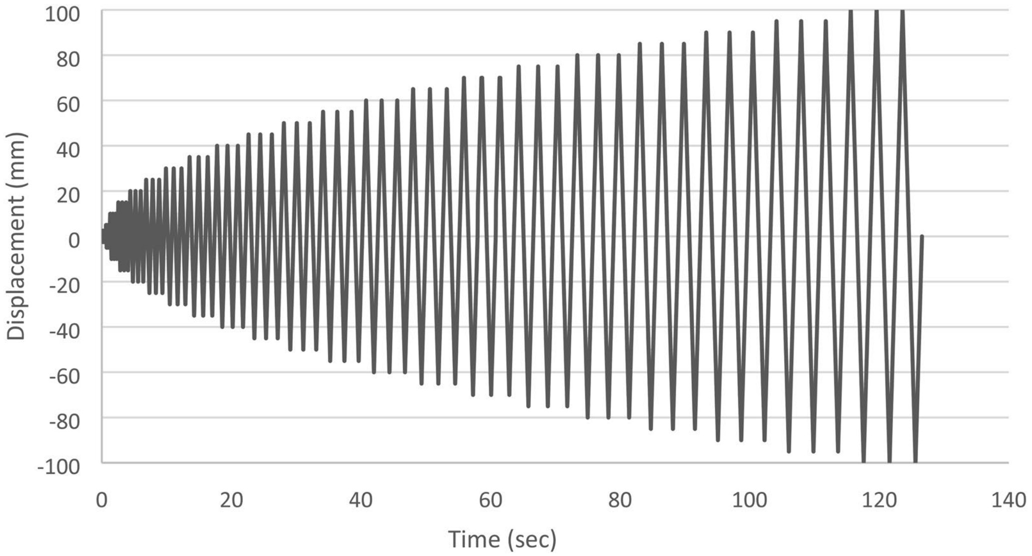

Fig. 5 Time vs. displacement amplitude (ACI Committee 374 2002)

surface to record the reinforcement strains during the entire testing. The averaged result of the two gauges would be used to compare the number of loads inflicted to the steel reinforcements between each specimen during the quasi-static cyclic tests. The breakdown of the set-up arrangement is depicted in Fig. 8.

5 Experimental Testing Results

In this section, five HyFRC and one plain concrete were cast on the joint region of a knee beam–column specimen for experimental testing. A total of six specimens were prepared and evaluated under lateral cyclic loadings for hysteresis behavior, displacement ductility, stiffness degradation rate, steel reinforcement strain, energy dissipation and cracking damage. The closing and opening action of the KJ under reversed cyclic loading was observed as illustrated in Fig. 9.

5.1 Hysteresis Response Results

The hysteretic behavior of the HyFRC beam–column joints at early load stages was similar to each other. The cracks which developed at the beam–column interfacial surface and near the joint–column interface continued to propagate extensively throughout the tests. The differences between plain concrete and the HyFRC were more apparent with large lateral displacements. The HyFRC produced higher maximum displacements, effective strength degradations, higher energy dissipation capacities and increased toughness (Fig. 10). Based on the hysteresis curves of the Control specimen, the knee beam–column joint was susceptible to more damages during the opening actions compared to the equivalent closing actions. The susceptibility is due to tensile stresses imposed on the outside corner joint of the beam–column specimen during the 'opening' or pulling action on the knee beam–column structure which caused brittle failure below the yield design moments (Angelakos 1999). The

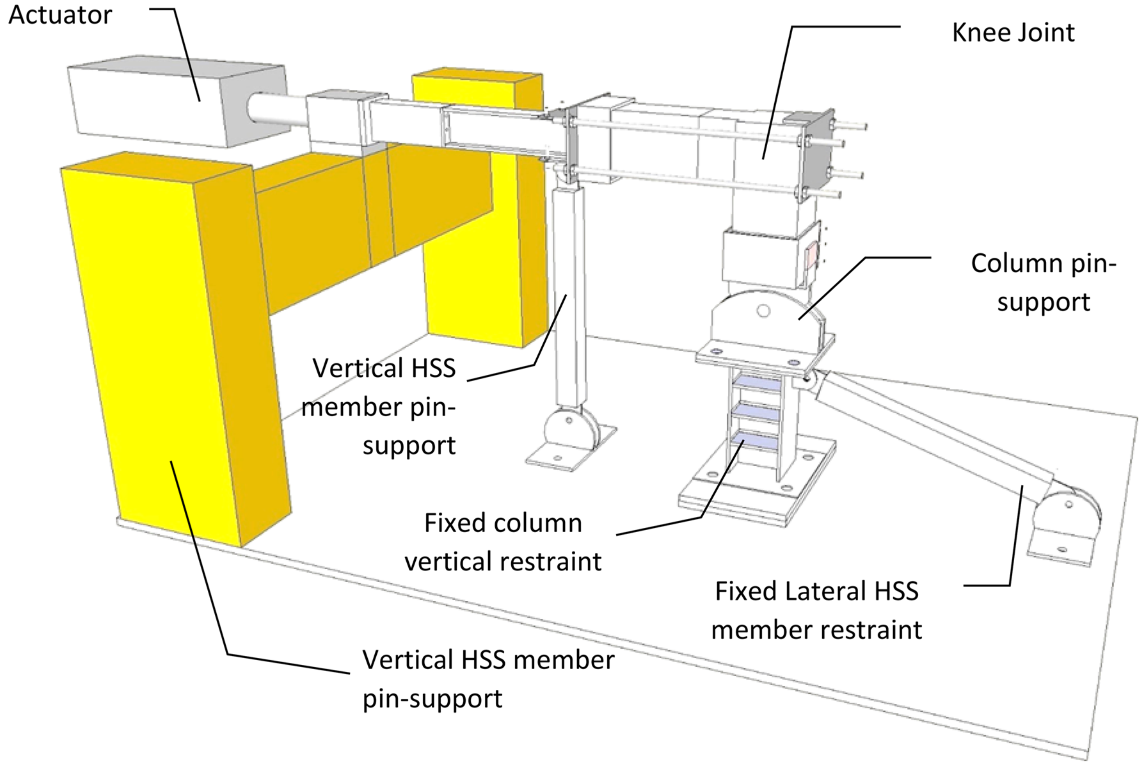

Fig. 6 Conceptual test set-up

Fig. 7 Experimental test set-up

damages caused at the inside corner subjected to compressive forces during closing actions were controllable because plain concrete is stronger in compression.

On the other hand, the F6U3, F6S3, F6E3 and F6N3 specimens achieved a higher maximum displacement compared to the Control and FFC specimens. During opening actions, the F6U3 produced a maximum displacement of 95 mm with a maximum load of 42 kN. While the F6S3 yielded a 91 mm displacement coupled with a 31 kN load, whereas, F6E3 yielded a 99 mm displacement at a 45 kN maximum load. The F6N3 managed to deform until it was displaced 99 mm with a 70 kN maximum load, which was higher than the other three maximum loads of the HyFRC joint specimens. However, the F6N3 also exhibited a brittle characteristic with a steep decline in the rate of strength degradation, while F6U3, F6S3 and F6E3 achieved a more gradual reduction in strength as lateral displacements increased. The FFC and Control specimens attained a lower final displacement, whereby the FFC yielded 79 mm deformation with a maximum load of 65 kN and the Control achieved a deformation of 74 mm with a 17 kN corresponding load. Both specimens produced a steep rate in strength degradation similar to that of the F6N3.

Additionally, during the closing actions, the F6U3, F6S3 and F6E3 specimens achieved a maximum displacement of 100 mm with corresponding final loads of 62 kN, 49 kN and 44 kN, respectively. The stated HyFRC produced a gradual decline in strength deterioration with every increase in lateral displacement. However, there was no observable improvement for the F6N3, FFC and C specimens as the strength degradation maintained a steep

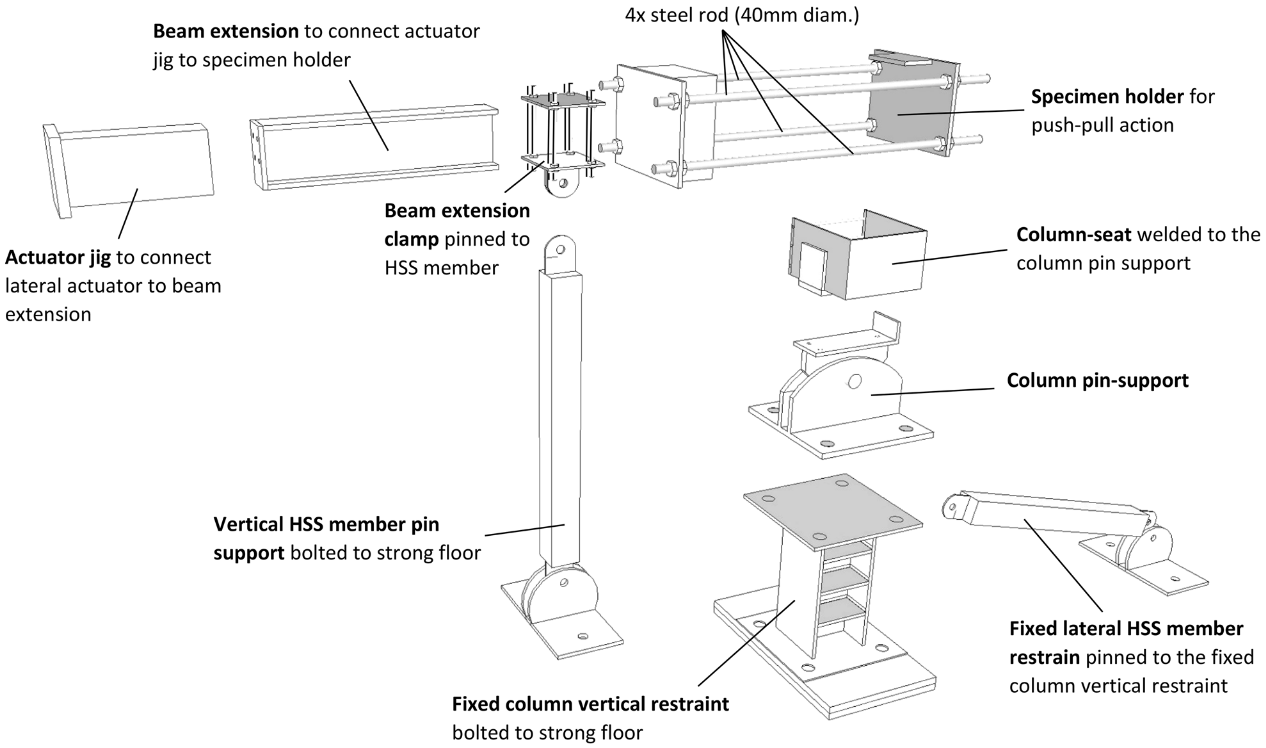

Fig. 8 Break down of experimental set-up arrangement

Fig. 9 The **a** closing and **b** opening action of knee beam–column joint

rate, similar to their behavior during opening actions. The F6N3 deformed until it reached a 98 mm deflection with a 142 kN load, while the FFC and C specimens achieved an 80 mm deflection coupled with a 101 kN load and a 79 mm deflection with a 102 kN maximum load, respectively.

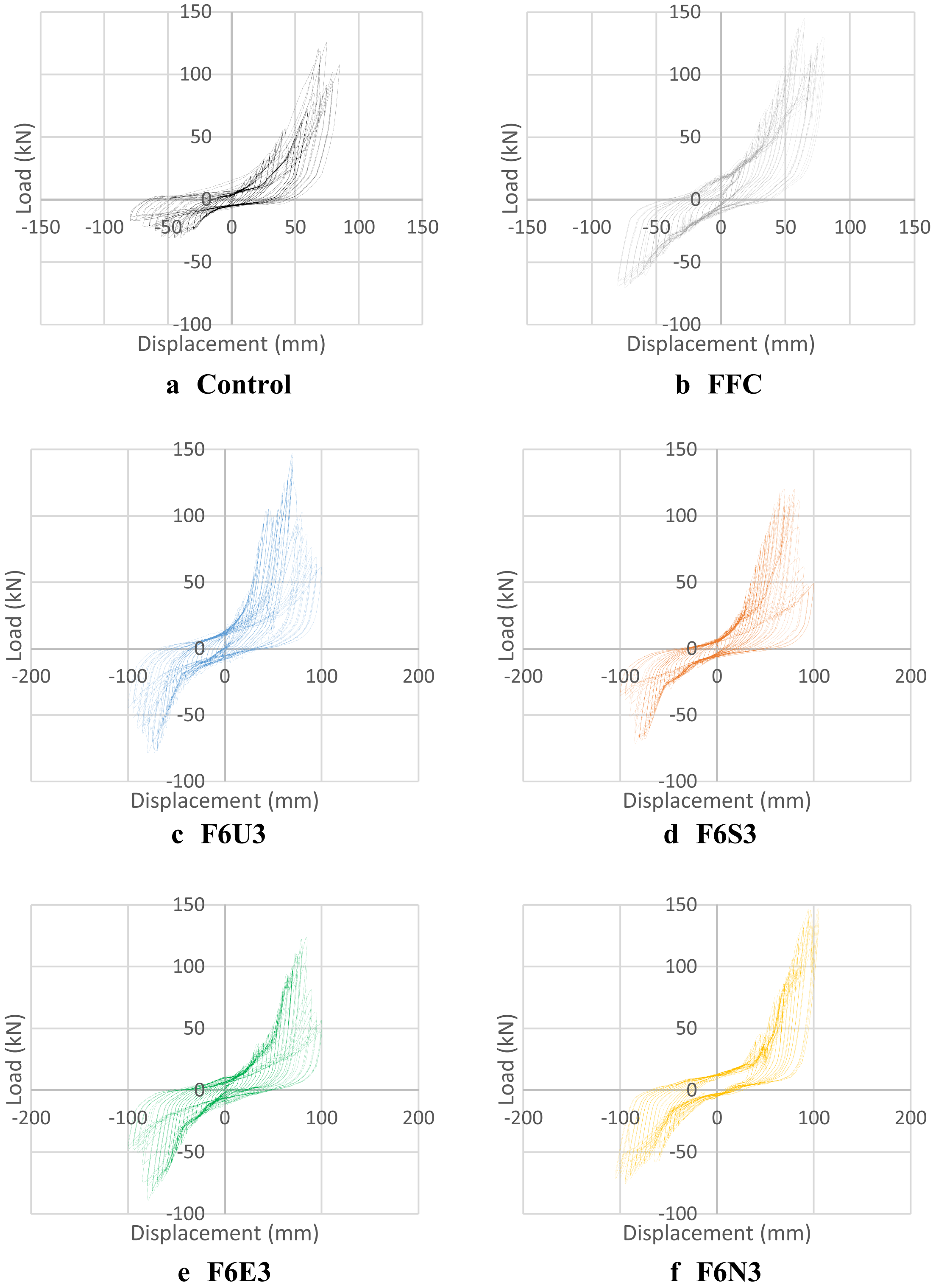

Fig. 10 Hysteresis curves of HyFRC knee beam–column joints

The hybrid combination of macro–micro-sized fiber (F6U3, F6S3, F6E3 and F6N3) in the joints were proven superior in improving the hysteretic behavior of the knee beam–column structural components compared to the conventional concrete (C) or macro-sized fibers (FFC) with the same ductile steel reinforcement detailing. The addition of HyFRC improved the KJ opening action under cyclic loadings by 28.38% for F6U3, 22.97% for F6S3, 35.14% for F6E3, 33.78% for F6N3 and 6.76% for FFC specimens. Moreover, the performance of the KJ during closing action was improved by 25.25%, 25.68%, 25.33%, 23.69% and 0.74%, respectively.

5.2 Envelope Curves

The envelope or backbone curve of the hysteresis loop was plotted (Fig. 11) to define the peak load response at difference displacement levels of the hysteresis curves. Polynomial curves were adopted to obtain an optimal trendline from the experimental data.

In the closing action's (+) elastic region, the F6U3, FFC and F6S3 specimens displayed superior peak load compared to the Control specimen. However, the trend was only applicable at low-level displacements, the FFC overtook the F6U3 at 45 mm displacement, while the Control specimens passed the F6S3 curves at 63 mm (Fig. 11). Subsequently in the opening act's (−) elastic region, the F6E3 obtained the highest peak load at smaller displacements, followed closely by the FFC specimen. The F6U3 specimen regained its strength at higher deformation levels, thus, intercepted F6E3 and FFC before it was subjected to peak load at 79 mm.

Meanwhile, the post-elastic region was where the HyFRC exceled in performance, especially for the micro–macro-fiber joint combinations. During the closing action (+), the developed F6U3, F6S3, F6E3 and F6N3 HyFRC joints displayed superior quasi-brittle characteristics in the post-crack regions. Their envelope curves extended to the 100 mm displacement threshold while still resisting loads. Although the FFC exhibited superior behavior in the elastic region, the curves failed at an 80 mm displacement threshold, close to the Control specimen's maximum displacement but inferior to the other HyFRC specimens.

Table 4 summarizes the respective peak loads and displacements for each of the knee beam–column specimens. Based on the data, the peak loads during opening actions improved substantially with the addition of HyFRC as a result of the fiber-bridging effects on the cracks. The increase was more than two times the peak load of the Control concrete, with the F6E3 achieving the highest peak load among all the developed HyFRC specimens. However, FFC yielded the least improvement highlighting the superior performance of F6U3, F6S3, F6E3 and F6N3 hybrid fibers in arresting micro- and macro-cracks during the testing. Microfibers were essential in increasing peak strength due to the concrete hardening effect it entails during the fiber-bridging effect at the microscopic level (Betterman et al. 1995). These multi-crack phenomena increase the peak stress of the HyFRC more than that of the FFC specimen.

The peak loads achieved during the closing action were not as significant as during the opening action. Although the F6N3 produced the highest peak load, the corresponding displacement was higher than the other HyFRC indicating a significant loss of stiffness in the elastic stage. The F6U3, F6E3 and FFC achieved peak loads at lower deformation levels, suggesting a gradual degradation of stiffness compared to the F6N3. The effects of stiffness degradation on the test specimens were further analyzed and discussed in Sect. 5.4. Additionally, the F6S3 resulted in a minimal decrease of 4.47% from Control concrete.

5.3 Displacement Ductility

The ratio of ultimate displacement for the knee beam–column joint displacement was calculated based on the envelope curves using the steps illustrated in Fig. 12. In addition, the toughness was calculated from the energy absorption capacity (area of the loop) of the hysteresis curves and are listed together with the obtained ductility in Table 5. The Control specimen exhibited the least displacement ductility compared to the rest of specimens with HyFRC joints. The improvement in displacement ductility produced by the F6U3 was the highest, while the FFC had the worst value compared to the rest of the specimens.

The difference in displacement ductility was caused by the variation in structural toughness, which directly affects the specimen's yield and ultimate displacement capacity. All of the HyFRC specimens indicated greater structural toughness than the Control specimen with the F6U3 being the most superior, followed by the F6S3, F6E3, F6N3 and the FFC as the lowest.

Based on Fig. 13, a direct correlation can be established between the toughness of the specimens and the overall displacement ductility of the knee beam–column structure. There is a significant increase in displacement ductility from the Control specimen to each of the HyFRC specimen, especially the F6U3 due to the superior toughness. The increase in toughness corresponds to an increase in displacement ductility except for the F6S3 specimen. Its displacement ductility was marginally higher even though the structural toughness was slightly lower than that of the F6E3 specimen.

The addition of the HyFRC into the joint has shown to increase the knee beam–column joint structural

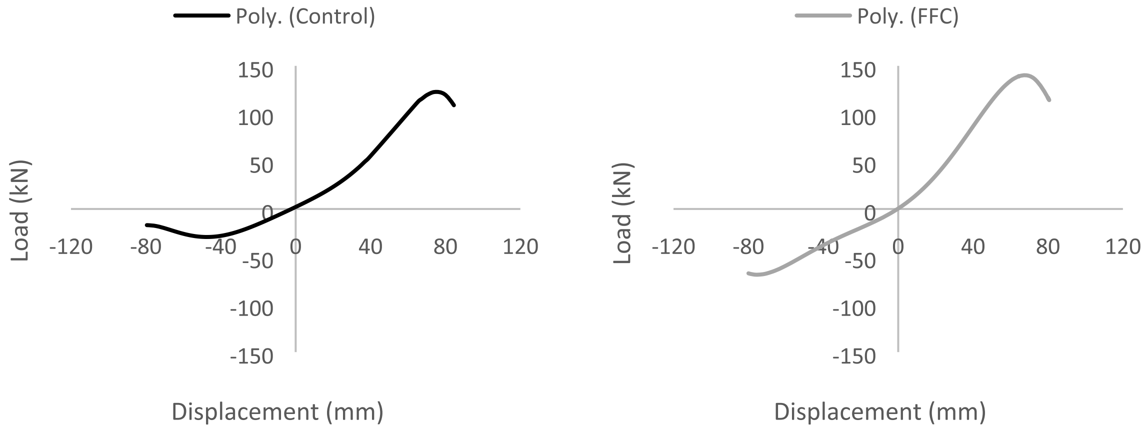

a Control **b** FFC

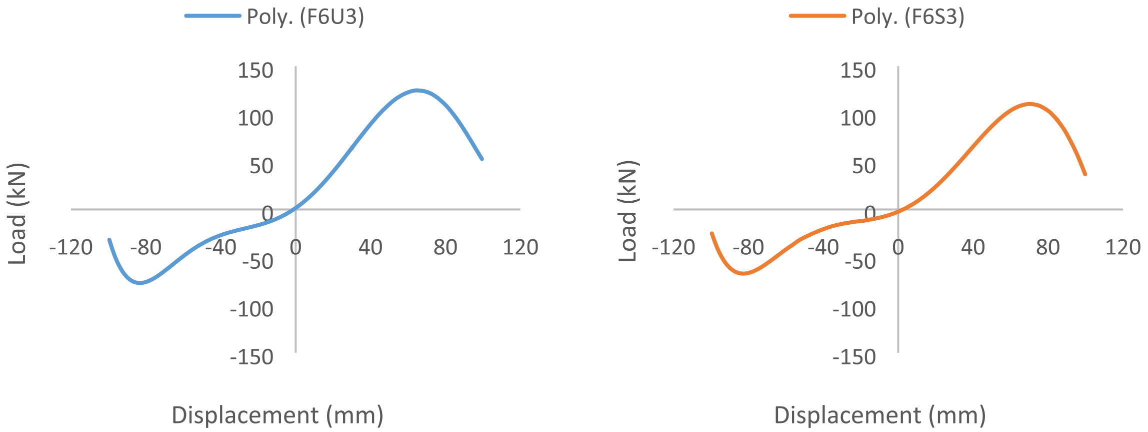

c F6U3 **d** F6S3

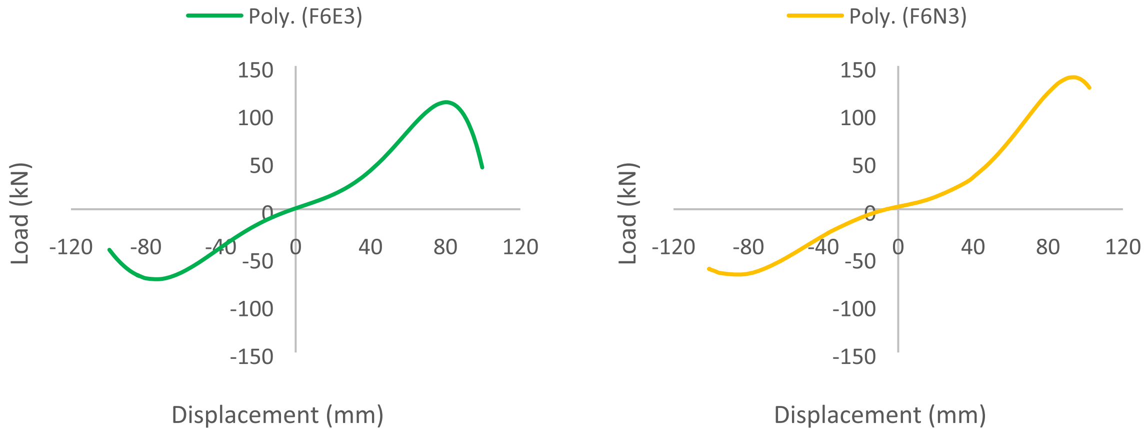

e F6E3 **f** F6N3

Fig. 11 Envelope curves for HyFRC beam–column specimens

Table 4 Peak loads and displacements

Specimen	Closing action (+)		Opening action (−)	
	Peak load (kN)	Displacement (mm)	Peak load (kN)	Displacement (mm)
Control	125.67	74.38	30.17	50.03
FFC	145.23	65.09	70.56	74.13
F6U3	146.89	69.62	78.50	79.2
F6S3	120.05	79.96	71.39	84.29
F6E3	123.60	84.28	89.42	79.23
F6N3	147.47	104.56	75.54	94.42

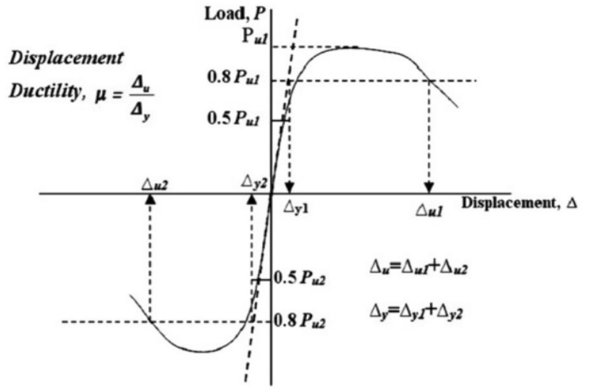

Fig. 12 Calculation for displacement ductility (Chidambaram and Agarwal 2015)

Table 5 Test results

Specimen	Total displacement		Displacement ductility, Δu/Δy	Toughness (kN-mm)
	Δu (mm)	Δy (mm)		
C	147	130	1.13	2612
FFC	155	115	1.35	3012
F6U3	180	110	1.64	8124
F6S3	159	106	1.50	6685
F6E3	172	121	1.42	7215
F6N3	176	125	1.41	5421

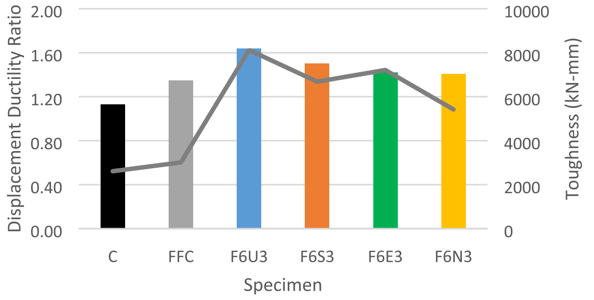

Fig. 13 Displacement ductility and toughness (Bar chart: displacement ductility ratio, Line graph: toughness)

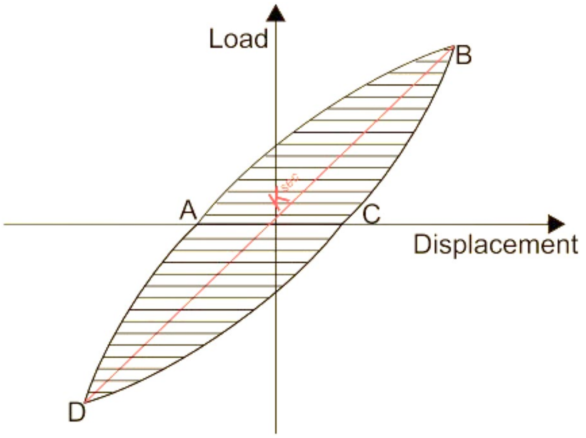

Fig. 14 Peak to peak secant stiffness calculation (Xue and Yang 2010)

toughness, which is as a result of the improved HyFRC residual strength and shear toughness caused by the polypropylene and nylon fibers in the post-cracking phase. These enhancements minimized excessive loads imposed on the steel reinforcements through the fiber-bridging effects on the propagating cracks. Hence, the yield and ultimate displacement of the knee structure during cyclic lateral loadings were improved.

5.4 Stiffness Degradation

The peak to peak secant stiffness (K_{sec}) of the Control and HyFRC specimens were measured from a straight line between the maximum loads and corresponding displacement points as illustrated in Fig. 14. According to Fig. 15, the knee beam–column joint using the developed HyFRC demonstrated higher initial stiffness compared to the Control specimen. Meanwhile, FFC yielded the highest improvement in initial stiffness by 41.67% compared to the Control specimen and the other HyFRC specimens. Followed by the F6U3 with a 30.83% improvement in stiffness at the initial displacement levels. The F6S3, F6E3 and F6N3 specimens only meagerly increased the

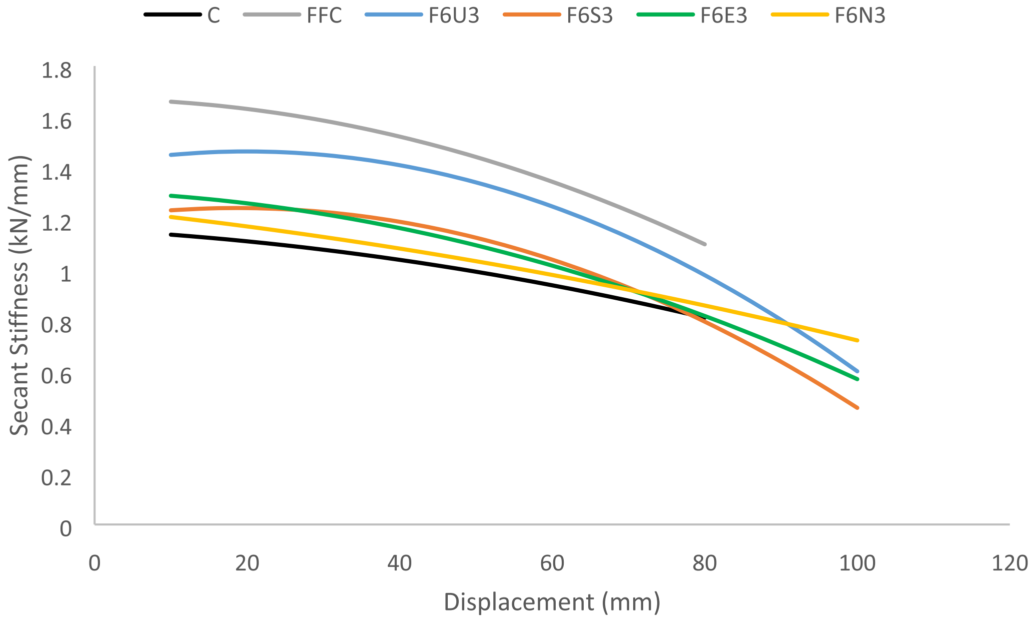

Fig. 15 Secant stiffness degradation

stiffness compared to the Control specimen with 7.5%, 8.33% and 3.33% improvements, respectively.

On the other hand, all of the specimens exhibited a low rate of change in degradation at early displacement levels with the Control producing the lowest degradation for the knee beam–column joints. Nevertheless, F6U3, F6S3, F6E3 and FFC specimens manifested a higher rate of change in stiffness at 40 mm displacement levels which continued to change to reach maximum displacements. As for specimen F6N3, a steep loss in stiffness was observed during early displacement and continued to degrade at a low rate of change, which subsequently exceeded the stiffness of F6S3 and F6E3 at 70 mm and the F6U4 at 90 mm displacement levels.

However, FFC was the stiffest among the HyFRC specimens, which is justified by the low displacement ductility and toughness results. The macro-sized HyFRC resulted in a high peak to peak stiffness at every displacement levels due to the effective crack fiber-bridging in the macroscopic range on the joints. Hence, the delay in the widening of crack-gaps minimized load directed to the steel reinforcement and also prevented bond-slip of the lateral steel reinforcements during the cyclic lateral load tests. Therefore, the secant stiffness degradation was improved.

The inclusion of microfibers in the F6U3, F6S3, F6E3 and F6N3 specimens resulted in higher displacement ductility and toughness for the knee beam–column joints but sacrificed the stiffness especially at higher displacement levels. Hence, it can be deduced that the microfibers in the hybrids resulted in high peak stress due to the multi-crack strain-hardening phenomenon of the concrete. Consequently, the secant stiffness of the HyFRC decreased because the physical limit of the Ferro macro-fibers exceeded due to the rapid propagation of the brittle crack. The sudden crack propagation into the post-peak region rendered the crack fiber-bridging action ineffective resulting in early slippage and yielding of steel reinforcements.

5.5 Steel Reinforcement Strain

The maximum strain for respective displacement levels of each specimen was calculated and plotted (Fig. 16) to observe the effects of the HyFRC joints on the performance of steel reinforcements on the developed knee beam–column joints under lateral cyclic loadings. Based on the curves, the control specimen yielded the highest strain during the tests, achieving a peak strain of 441 με in the pushing direction and 471 με in the pulling direction. A large amount of loads were transferred to the joint steel reinforcement leading to higher strain and reduced resistance during the early displacements as a result of the premature concrete failure.

On the other hand, the injection with the developed HyFRC in the joints reduced the strain significantly. However, F6U3 exhibited the lowest steel reinforcement strain with 87 με (the highest strain) in the pushing direction and 187 με in the pulling direction. The hybrid combination for this specimen reduced the strain on the joints steel reinforcement by 80.27% in pushing and

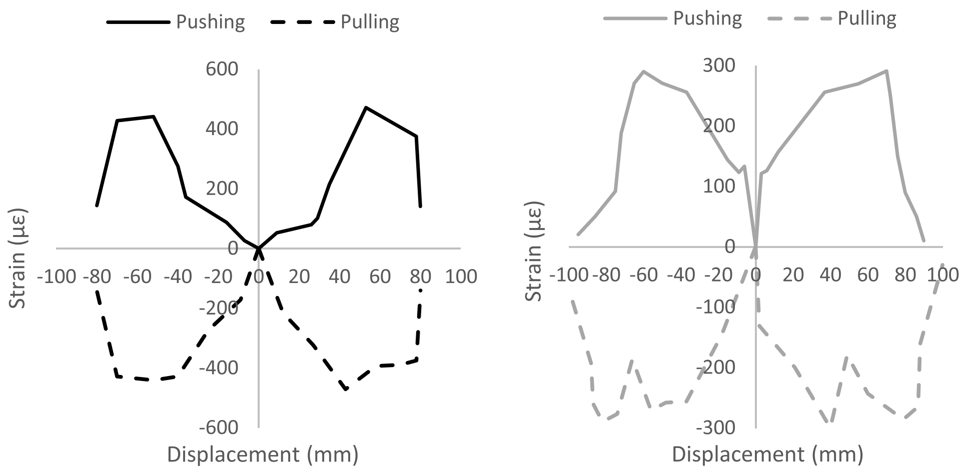

a Control **b FFC**

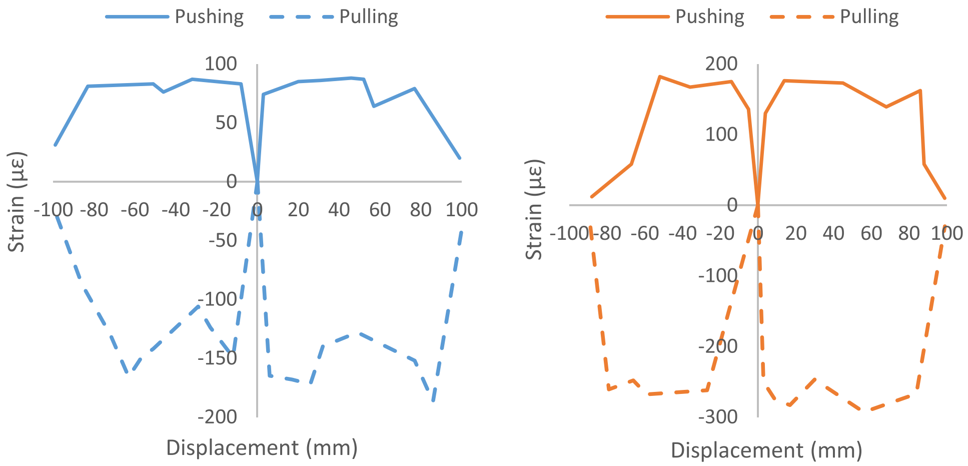

c F6U3 **d F6S3**

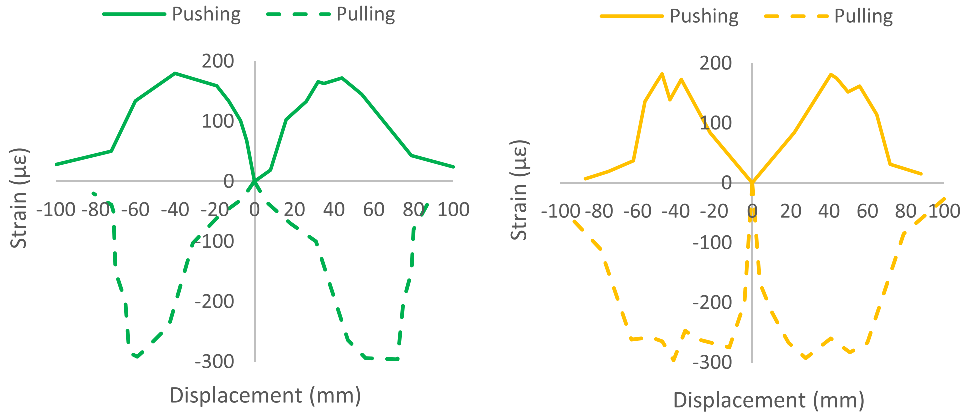

e F6E3 **f F6N3**

Fig. 16 Steel reinforcements strain data

60.30% in the pulling directions. meanwhile, the performances of the F6S3, F6E3 and F6N3 were almost similar with each other, in which all three achieved peak strains lower than 200 με and 300 με in the pushing and pulling directions, respectively.

The fiber-bridging effect of the fibers was very effective in limiting the loads inflicted to the steel reinforcement on the joint. The effect delayed the reinforcement failure which governed the structural toughness, displacement ductility and stiffness degradation rate of the knee beam–column joint. However, at high displacement levels, the physical limitation of the fibers exceeded, subsequently resulting in breakage of the fibers.

Moresoever, premature steel reinforcement slippage of the beam from the connection might have occurred as a result of the flexural yielding of reinforcements (Siva Chidambaram and Agarwal 2018). The steel reinforcement hinges during the testings clarified the declining strain upon reaching the specimen's maximum displacement capacity.

Meanwhile, F6N3 demonstrated slightly reduced stiffness of steel reinforcement during the early displacement levels in the pushing direction. The reduction in stiffness was due to the weakening of the compressive strength of the developed material,the combination of the Ferro macro-fiber and Nylo-Mono microfibers. These fibers decreased the compressive strength of conventional concrete, resulting in higher loads transferred to the steel reinforcement joint due to early concrete failure. Nevertheless, the improvement in compressive toughness supported the residual strength to reduce the strains on the reinforcements, which is evident from the larger displacements levels.

It can also be deduced that specimens F6U3, F6S3, F6E3 and F6N3 which were a combination of the macro–micro-class fibers, to be superior in performance than using macro-fiber only fibers as exhibited by the FFC specimen. The FFC yielded maximum (highest among the HyFRC specimens) reinforcement strain of 291 με in the pushing direction and 300 με in the pulling direction. In the pushing direction, F6U3 further improved the reduction in steel reinforcement of the FFC by 70.10%, F6S3 by 37.46%, F6E3 by 38.14% and F6N3 by 37.80%. Besides that, in the pulling direction, the improvements were in the range of 37.67% for F6U3, 2.33% for F6S3, 1.33% for F6E3 and 1.17% for F6N3.

5.6 Energy Dissipation

The energy dissipation capacity is a crucial parameter to measure the knee beam–column joint's toughness before failure. It governs the ductile response of the structure in its post-yield response, whereby the results determine the efficiency of the developed HyFRC as the joint material throughout the lateral cyclic loading. The cumulative energy dissipation capacity measures the total energy after each subsequent cycle. It is calculated from the area of the loop in the hysteresis curves. Figure 17 displays the energy dissipation capacity for each specimen with respect to displacement levels.

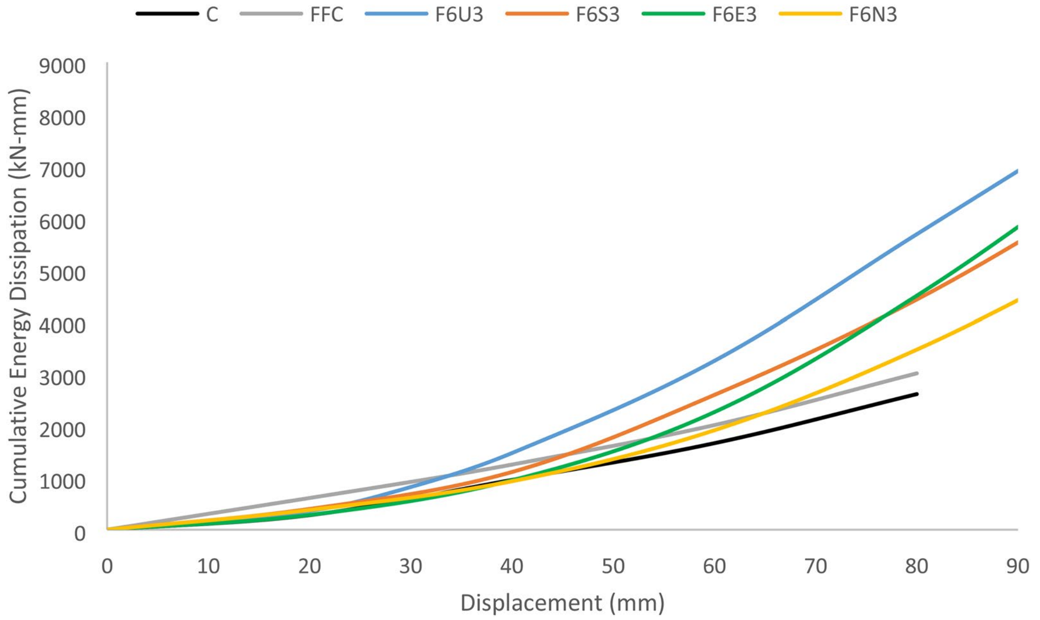

Fig. 17 Cumulative energy dissipation

All of the developed HyFRC exhibited better ductile structural response than the Control specimen. The F6U3 has an energy dissipation rate of 3.11 times higher than the Control specimens and is considered the highest among all the test specimens. Meanwhile, the performances of the F6E3 and F6S3 were meagerly similar, with F6S3 releasing more energy at early displacement levels up to 77 mm deformation levels, whereby, F6E3 exceeded the value to reach its maximum displacement level. Moreover, F6E3, F6S3 and F6N3 improved the energy dissipation of the structure by 2.76, 2.56 and 2.08 times the capacity of the plain concrete.

It was also observed that FFC produced the lowest dissipation capacity among all the HyFRC specimens, only improving the Control specimen dissipation rate by 1.15 times. The efficiency of using dual-class fibers in dispersing energy was proven to be superior to using macro-fibers-only hybrid especially in improving the toughness of the structure. The improved material toughness provided by the microfibers ensure a gradual pull-out of macro-fibers during the fiber-bridging effect. A frictional pull-out of macro-fibers is more desirable than fiber-breakage due to the high rate of energy dissipation, which contributes to the dissipation capacity of the overall structure. However, it also limits the inducement of large strains to the steel reinforcements on the joints by improving toughness. In conclusion, F6U3 yielded the best performance followed by the F6E3, F6S3, F6N3, FFC and C (the worst).

5.7 Cracking Damage

In early loading stages, all specimens behaved similarly with flexural cracks developing at the joint–beam interface just outside the joint core region. As the displacement increased, horizontal cracks were observed at the joint–column interface which further propagated and coalesced with the cracks encapsulating the beam. The flexural cracks that were formed concentrated at the plastic hinge of the beam section.

The damage on the beam–column joint for all specimens are displayed in Fig. 18. The Control specimen experienced the highest damage during the testing and exhibited concrete spalling on the joint–column region. Specimen FFC also exhibited similar damage as the Control specimen but in a slightly lower intensity. Meanwhile, F6U3, F6S3, F6E3 and F6N3 specimens resulted in fewer cracks and damages compared to the C and FFC specimens due to their superior HyFRC crack fiber-bridging capabilities.

6 Numerical Simulation

6.1 Convergence Mesh Study

A mesh convergence study was conducted to determine the most suitable mesh size to be applied to the FE beam–column joint models in this study. Five global mesh were modeled and compared against the experimental data for the Control specimen (C mix-design). The loading history in Fig. 5 was used to conduct the study. The skeleton curves were extracted from the hysteresis plots obtained from the numerical analyses as indicated in Fig. 19. Table 6 displays the percentage differences in peak load, peak load displacement, and maximum displacement of the FE model in the opening and closing action of KJ.

Based on the results, GB40 and GB20 mesh sizes produced a much higher accuracy of hysteresis behavior to the experimental data with percentage differences of less than 10% in all the parameters. However, the processes involved in extracting all required data were computationally taxing and time-consuming. Furthermore, the models were only using plain concrete with simplified Concrete Damaged Plasticity (CDP) properties in the plastic stage. On the occasion that the developed HyFRC in this study were to be implemented on the joint using complex CDP properties, the expected FE analyses would be tremendously taxing and demands higher computational processing power.

Finally, GB60 mesh size was chosen for all FE models. The accuracy of the models from the experimental data was less than 30% which were within an acceptable range. The FE analyses were computationally less taxing and the time taken to complete a full model analysis was within reasonable duration for normal concrete beam–column joints. The GB60 mesh size was selected to balance the computational power required in analyzing the HyFRC KJs under lateral cyclic loading and the total time required to complete a full analysis with data extraction.

6.2 Modeling Design

The FE of the KJ was developed using the ABAQUS finite element commercial software for numerical simulation. Constitutive modeling was conducted for all five HyFRC materials developed in this study. The experimental uniaxial compression and tensile tests that were previously conducted (Zainal et al. 2020b) were considered for strain-hardening and strain-softening branch of the materials. The data are used as input the Concrete Damage Plasticity section in Abaqus FEM. The accuracy of the FE models was validated by comparing the results obtained from the numerical analyses with the experimental tests. A uniform mesh of 50 mm was designed for the beam–column concrete model along with its embedded steel reinforcements are depicted in Fig. 20a, b. This configuration resulted in a total of 1252 nodes

a **Control** **b** **FFC**

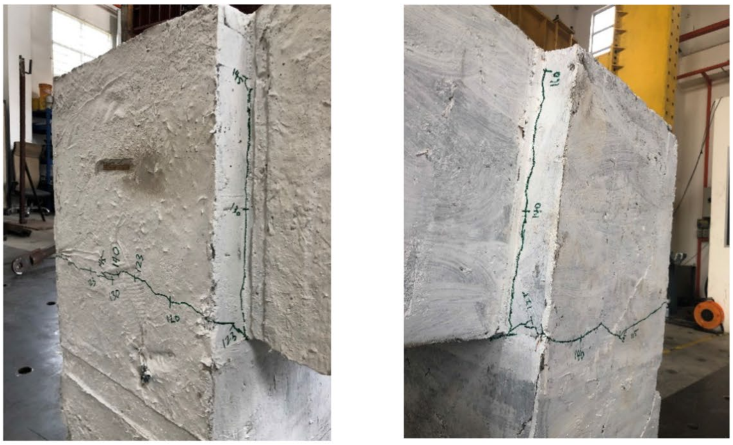

c **F6U3** **d** **F6S3**

e **F6E3** **f** **F6N3**

Fig. 18 Damage in the joint region

and 1216 elements for the steel reinforcements and 3024 nodes with 2176 elements for the knee RC beam–column joints. Specific details on the elements used are presented in Table 7.

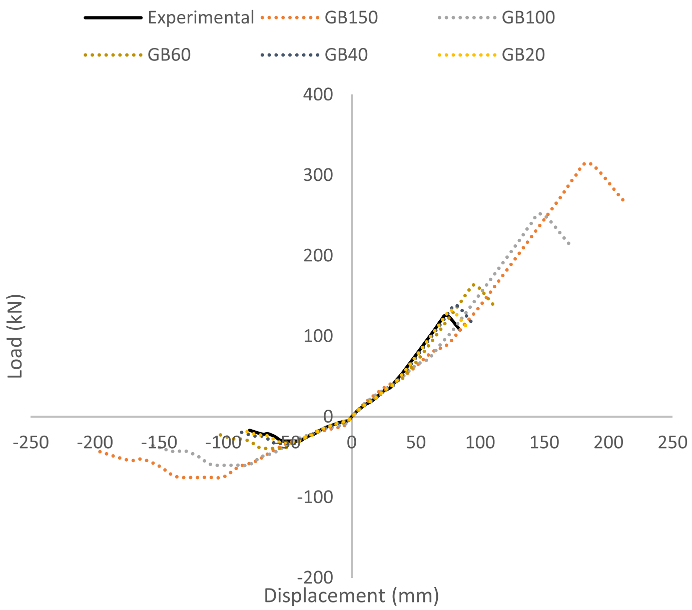

Fig. 19 Comparison between the numerical model and experimental data

Figure 21 illustrates the pinned-type supports defined at the base of the column (RP-3) and the surface of the beam (RP-1). The base of the column restrains any type of movement except for rotation on the x-axis, while the surface of the beam only allows lateral movement in the z-axis. The beam and column were attached to the HyFRC joint via tie-type constraints. A displacement-controlled loading was introduced to the beam surface at point RP-1. Meanwhile, the cyclic loading moved in the z-axis direction with a factor of 1 from the pre-designated tabular amplitude. The amplitude used was similar to the experimental tests illustrated in Fig. 5.

The materials used in the beam–column model comprised of a combination of plain and fibrous concrete. Both materials were defined to possess a 0.2 Poisson's ratio and 2400 kg/m^3 density. Young's modulus for plain concrete was adopted from the standard Eurocode 2: Design of Concrete Structures at 30 GPa (BS EN 1992–2:2005 2005). Additionally, Young's modulus for the developed HyFRC was experimentally obtained at 34

Table 6 Accuracy of mesh model against experimental data in closing and opening action

Mesh global size	Total elements	Peak load (kN)	Percentage difference (%)	Peak load displacement (mm)	Percentage difference (%)	Max. displacement (mm)	Percentage difference (%)
Closing action (+)							
GB150	126	314.19	85.71	185.95	85.71	211.25	85.71
GB100	332	251.35	66.67	148.76	66.67	169.00	66.67
GB60	1379	163.38	26.09	96.69	26.09	109.85	26.09
GB40	4280	138.24	9.52	81.82	9.52	92.95	9.52
GB20	33,480	131.96	4.88	78.10	4.88	88.72	4.88
Opening action (−)							
GB150	126	75.64	85.71	122.98	85.71	198.72	85.71
GB100	332	60.51	66.67	98.38	66.67	158.98	66.67
GB60	1379	39.33	26.09	63.95	26.09	103.34	26.09
GB40	4280	33.28	9.52	54.11	9.52	87.44	9.52
GB20	33,480	31.77	4.88	51.65	4.88	83.46	4.88

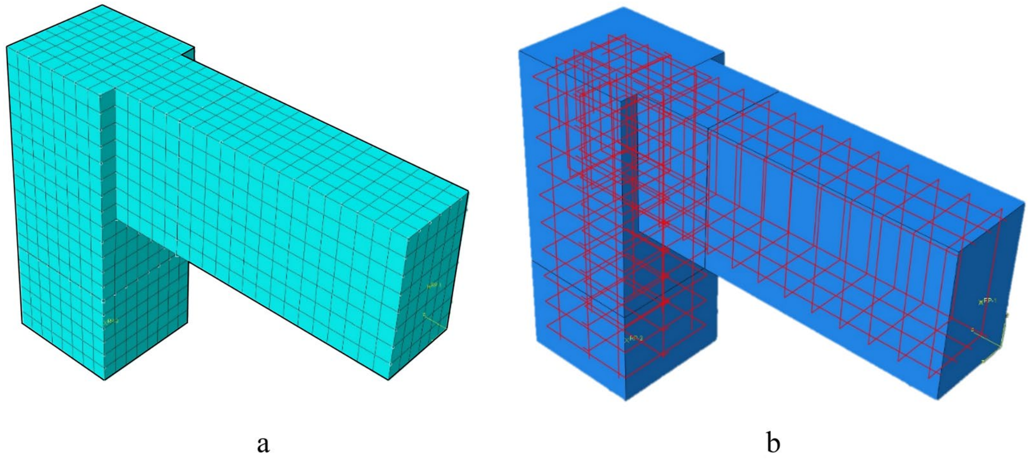

Fig. 20 RC knee beam column **a** mesh and **b** embedded steel reinforcements

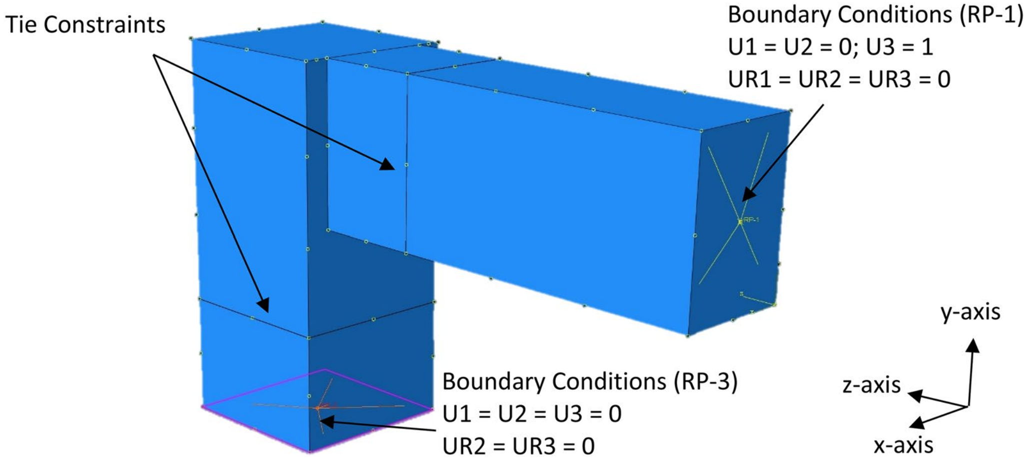

Fig. 21 Boundary conditions in FE models

Table 7 Elements used for RC beam–column models

Model	Element type	Element shape	Geometrical order	No. of elements
RC Knee Connection	C3D8R	Hexahedral	Linear	2176
Steel Reinforcement	B31	Line	Linear	1216

GPa. The ABAQUS default values chosen for the Concrete Damaged Plasticity (CDP) parameters are listed in Table 8.

The hysteresis responses are depicted in Fig. 22 and the results are tabulated in Table 9. In the closing action (+), the F6U3 numerical model exhibited the least accurate peak load percentage differences with a 31.31% difference from its experimental result. The most accurate model was the FFC with a minimal difference of 12.12%. Specimens F6S3, F6E3 and F6N3 resulted in percentage differences of 30.05%, 29.10% and 26.82%, respectively. However, FFC displayed the highest difference (8.98%) in the peak load–displacement, followed by the F6S3 model with a 6.03% margin difference. Models F6U3, F6E3 and F6N3 were very accurate with a percentage margin of

Table 8 CDP Abaqus default values

Plasticity parameters	Notation	Default value
Dilation angle	ψ	31°
Eccentricity	ϵ	0.1
Stress ratio	fb_0/fc_0	1.16
Shape factor	K	0.667
Viscosity parameter	μ	0

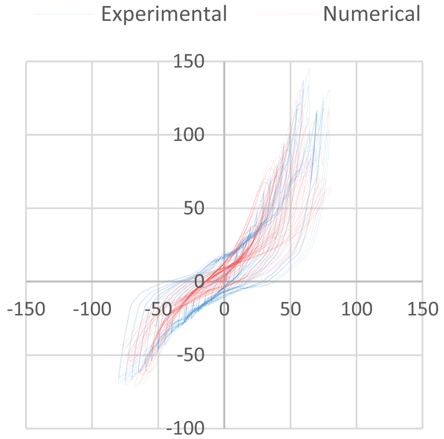

a FFC

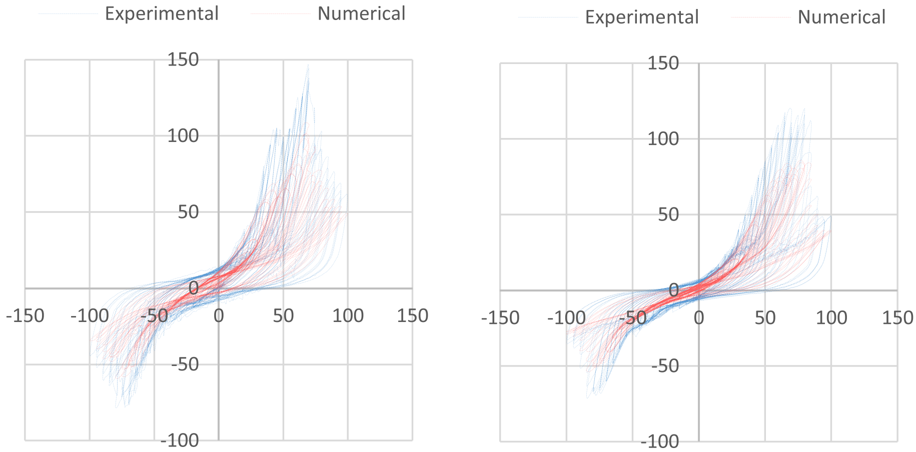

b F6U3

c F6S3

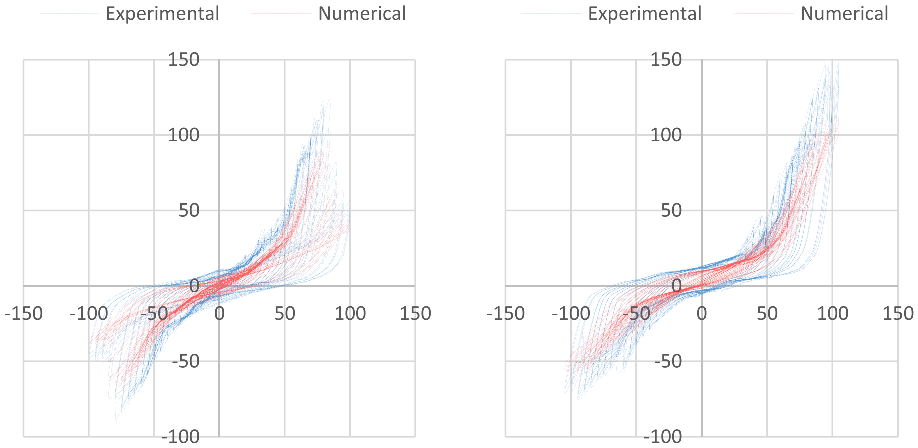

d F6E3

e F6N3

Fig. 22 Numerical vs. experimental hysteresis curves

below 1%. Likewise, all FE models depicted insignificant percentage differences in the maximum displacement capacity, with a margin of error below 1%.

In the opening action (−), the numerical model simulated the same weak load-carrying ability when the KJ flexes outwards, as opposed to inwards. The most accurate model was the FFC with only a 2.15% percentage difference. While, F6U3, F6S3, F6E3 and F6N3 displayed error margins of below 30% which are 28.28%, 29.46%, 20.50% and 25.98% correspondingly. For the peak load displacement, the highest difference was achieved by the FFC model with a 15.16% error margin from the experimental data. It was also observed that the percentage differences for every other model namely the F6U3, F6S3, F6E3 and F6N3 were very minimal. F6U3 yielded an error margin of 1.74%, while the rest were below 1%. In addition, the highest maximum displacement percentage difference was achieved by the FFC model with a 4.54% difference, followed by F6U3 model with a 1.21% variation from the experimental data. All the F6S3, F6S3 and F6N3 FE models displayed error margins below 1% compared to their experimental data.

A polynomial curve fitting technique was used to provide the best envelop curve trend lines for each of the models as depicted in Fig. 23. All numerical FE models adopted the sixth-order polynomial curves as tabulated in Table 10 for comparison. The correlation factor between the experimental and numerical models indicated very minimal differences, in the range of 98%. A good line of fit can, therefore, be deduced between the load and displacement variables based on the positive correlation.

Figure 24 displays the damages on the proposed FE numerical models under quasi-static cyclic testing. A majority of the damages inflicted on the core joint region were observed from the diagonal shear damage. The FFC model suffered the most shear damages in the joint region followed by the F6N3 model. Less damage was observed for the F6U3, F6S3 and F6E3 models. In the beam section, flexural damage was observed on top of the beam–joint interfacial surface, while horizontal damages were detected on the joint–column surface for all FE models.

The damages in the numerical models were slightly different from the crack pattern exhibited by the specimens during the experimental testing. The flexural damages in the FE models developed on the top of the joint–beam surface as opposed to the bottom in the experimental testing. Furthermore, no shear cracks were observed in the joint region during the experimental tests. Only flexural cracks on the joint–beam surface and horizontal cracks were observed on the joint–column surface.

Table 9 Knee joint experimental and numerical comparison in closing and opening actions

Specimen	Verification	Peak load (kN)	Percentage difference (%)	Peak load displacement (mm)	Percentage difference (%)	Maximum displacement (mm)	Percentage difference (%)
Closing action (+)							
FFC	Experimental	128.56	12.18	59.45	8.98	80.03	0.30
	Numerical	145.24		65.04		80.27	
F6U3	Experimental	146.86	31.31	69.62	0.47	99.50	0.30
	Numerical	107.10		69.95		99.80	
F6S3	Experimental	120.03	30.05	79.96	6.03	99.85	0.03
	Numerical	88.67		84.93		99.82	
F6E3	Experimental	123.60	29.10	84.28	0.78	99.64	0.12
	Numerical	92.20		84.94		99.76	
F6N3	Experimental	147.47	26.82	104.56	0.99	104.75	0.14
	Numerical	112.60		103.53		104.60	
Opening action (−)							
FFC	Experimental	69.07	2.15	79.19	15.16	79.99	4.54
	Numerical	70.57		68.03		76.44	
F6U3	Experimental	78.50	28.28	79.21	1.74	99.83	1.21
	Numerical	59.05		77.84		98.63	
F6S3	Experimental	71.39	29.46	84.29	0.79	99.85	0.33
	Numerical	53.06		84.96		99.52	
F6E3	Experimental	89.42	20.50	79.23	0.46	99.81	0.31
	Numerical	68.92		78.87		99.50	
F6N3	Experimental	75.54	25.98	94.42	0.79	104.74	0.01
	Numerical	58.17		93.68		104.73	

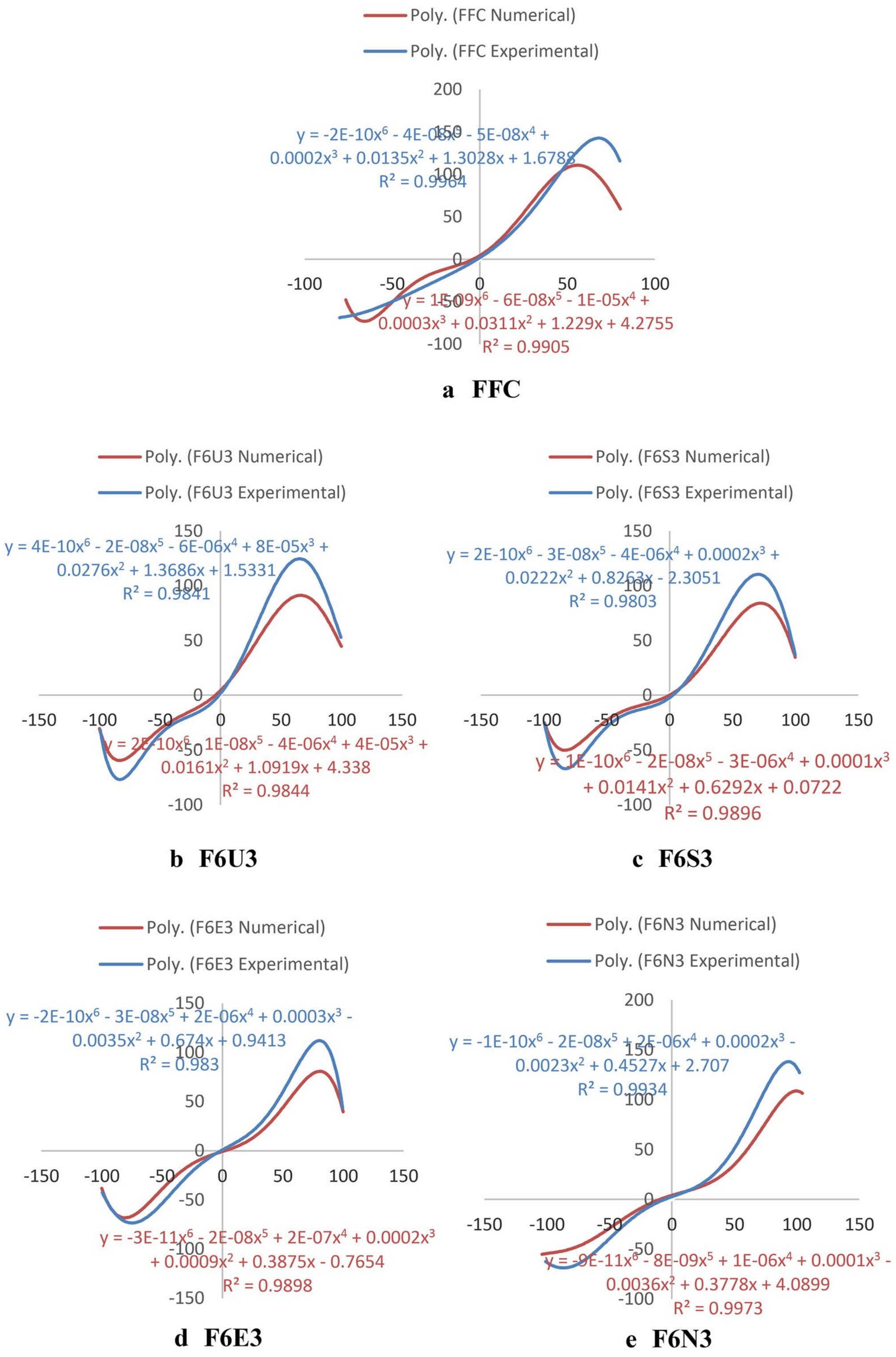

a FFC

b F6U3

c F6S3

d F6E3

e F6N3

Fig. 23 Numerical vs experimental envelope curves

Table 10 Trend line comparison

Specimen	Test	Trend line equation	Correlation factor
FFC	Experimental	$y = -2E-10x^6 - 4E-08x^5 - 5E-08x^4 + 0.0002x^3 + 0.0135x^2 + 1.3028x + 1.6788$	0.9964
	Numerical	$y = 1E-09x^6 - 6E-08x^5 - 1E-05x^4 + 0.0003x^3 + 0.0311x^2 + 1.229x + 4.2755$	0.9905
F6U3	Experimental	$y = 4E-10x^6 - 2E-08x^5 - 6E-06x^4 + 8E-05x^3 + 0.0276x^2 + 1.3686x + 1.5331$	0.9841
	Numerical	$y = 2E-10x^6 - 1E-08x^5 - 4E-06x^4 + 4E-05x^3 + 0.0161x^2 + 1.0919x + 4.338$	0.9844
F6S3	Experimental	$y = 2E-10x^6 - 3E-08x^5 - 4E-06x^4 + 0.0002x^3 + 0.0222x^2 + 0.8263x - 2.3051$	0.9803
	Numerical	$y = 1E-10x^6 - 2E-08x^5 - 3E-06x^4 + 0.0001x^3 + 0.0141x^2 + 0.6292x + 0.0722$	0.9896
F6E3	Experimental	$y = -2E-10x^6 - 3E-08x^5 + 2E-06x^4 + 0.0003x^3 - 0.0035x^2 + 0.674x + 0.9413$	0.9830
	Numerical	$y = -3E-11x^6 - 2E-08x^5 + 2E-07x^4 + 0.0002x^3 + 0.0009x^2 + 0.3875x - 0.7654$	0.9898
F6N3	Experimental	$y = -1E-10x^6 - 2E-08x^5 + 2E-06x^4 + 0.0002x^3 - 0.0023x^2 + 0.4527x + 2.707$	0.9934
	Numerical	$y = -9E-11x^6 - 8E-09x^5 + 1E-06x^4 + 0.0001x^3 - 0.0036x^2 + 0.3778x + 4.0899$	0.9973

The differences in crack pattern behavior of the FE analyses with the experimental results are partly due to the constitutive modeling of the developed HyFRC obtained from the uniaxial compression and tensile tests. The Abaqus CDP properties only entailed a minimum requirement of uniaxial testing of a developed material to obtain the compressive and tensile stress–strain curves as input for the FE software (Simulia 2001). However, this study did not conduct biaxial and triaxial tests of the proposed materials and only used the Abaqus default values depicted in Table 8. The behavior of the constitutive models developed for the HyFRC in stiffness recovery, softening behavior, degradation rate and rate sensitivity were precise with slight differences in results (Hashim et al. 2020).

Furthermore, due to the nature of complicated experimental set-up for L-shaped knee beam–column joint specimens, the boundary conditions defined on the experimental set-up might be exposed to several limitations. The fixed vertical and horizontal restraint shown in Fig. 6 were subjected to slight translational movements as a result of the cyclic push–pull of the actuator. This indirectly affects the capability of the fixed support to tightly anchor the column base. In addition, the set-up of the experimentation involved several fabricated jigs as shown in the breakdown in Fig. 8. The jigs were fabricated separately and were only welded to together during the assembling and positioning of the set-up, to comply and readjust with available equipment in Universiti Putra Malaysia's structural laboratory. The 40 mm steel rods on the specimen holder may have resisted the push–pull loads from the actuator, strengthening the experimental specimens slightly from the FE numerical models results. Furthermore, the beam extension clamp connecting the beam extension to the vertical HSS member pin support were also exposed to some degree of freedom because of the eccentricity of the boundary conditions. It was also observed that there were slight gaps inside the column pin support provided in the structural laboratory, which allowed slight movement to the sides during the lateral front–back movement of the push–pull action. This may have altered the cracking pattern and mode of failure of the RC specimens as opposed to a controlled set-up in FE modeling.

7 Concluding remarks

This study attempted to develop HyFRC using multiple synthetic fibers to enhance the performance of knee beam–column joints. Five different types of HyFRC materials were introduced to the joint region to limit the inducement of large strains to the steel reinforcements and improve the overall ductility of the KJ structure. The developed HyFRC consisted of a combination of several FORTA Corporation (Grove City, PA, USA) synthetic fibers namely the Ferro, Ultra-Net, Super-Net, Econo-Net and Nylo-Mono fibers. Experimental tests were conducted for six KJ specimens with five HyFRC and one Control specimen under lateral reversed cyclic loading. The proposed Finite Element KJ models were then verified using the data obtained from the experimental tests to measure the accuracy of the developed numerical models. The summary of the findings is as follows:

- The opening action of the KJ was improved by 8.38% for the Ferro-Ultra hybrid, 22.97% for the Ferro-Super hybrid, 35.14% for the Ferro-Econo hybrid, 33.78% for the Ferro-Nylo hybrid and 6.76% for the Ferro-Ferro hybrid. Likewise, the closing action of the KJs was enhanced by 25.25% for the Ferro-Ultra hybrid, 25.68% for the Ferro-Super hybrid, 25.33% for the Ferro-Econo hybrid, 23.69% for the Ferro-Nylo hybrid and 0.74% for the Ferro-Ferro hybrid.

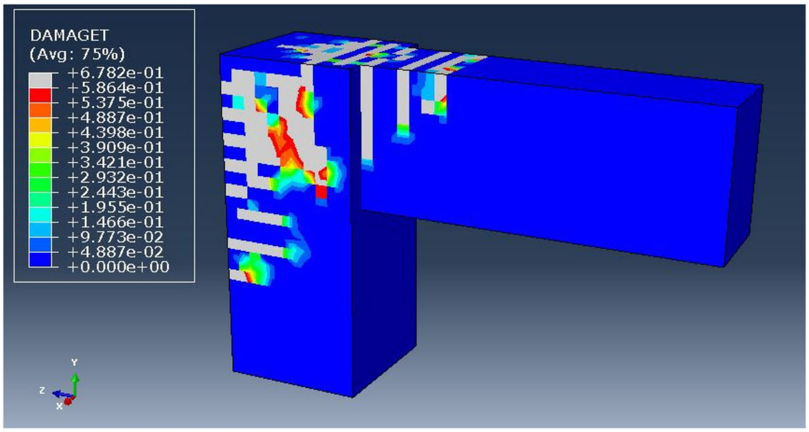

a FFC damage in FE model.

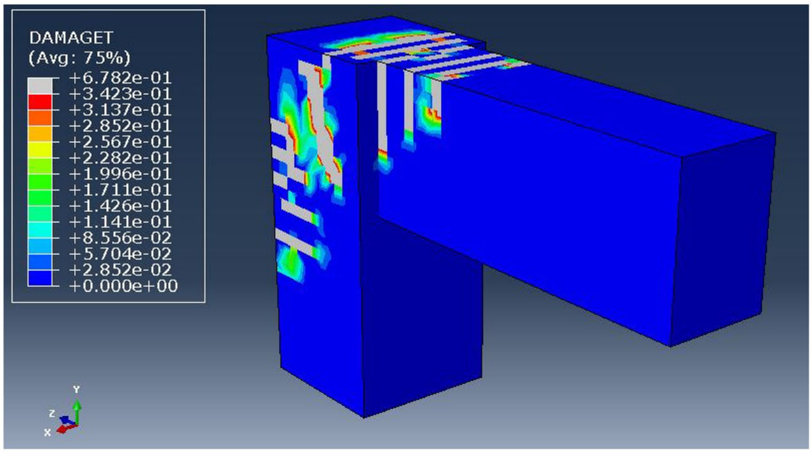

b F6U3 damage in FE model.

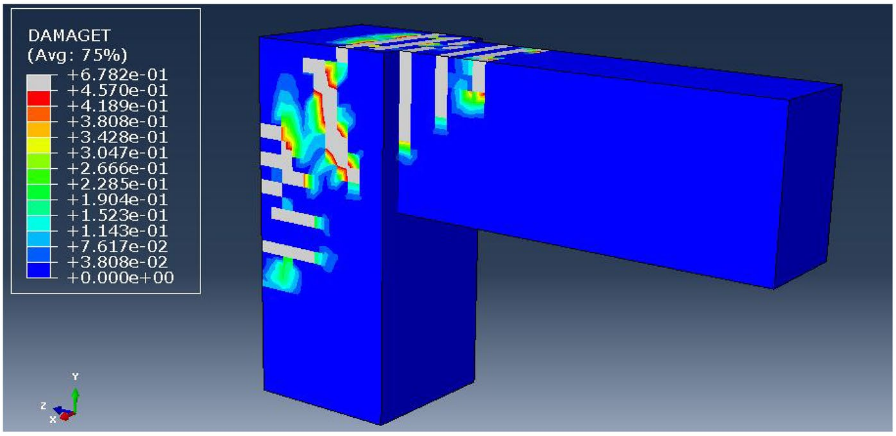

c F6S3 damage in FE model.

Fig. 24 Damage in proposed FE models

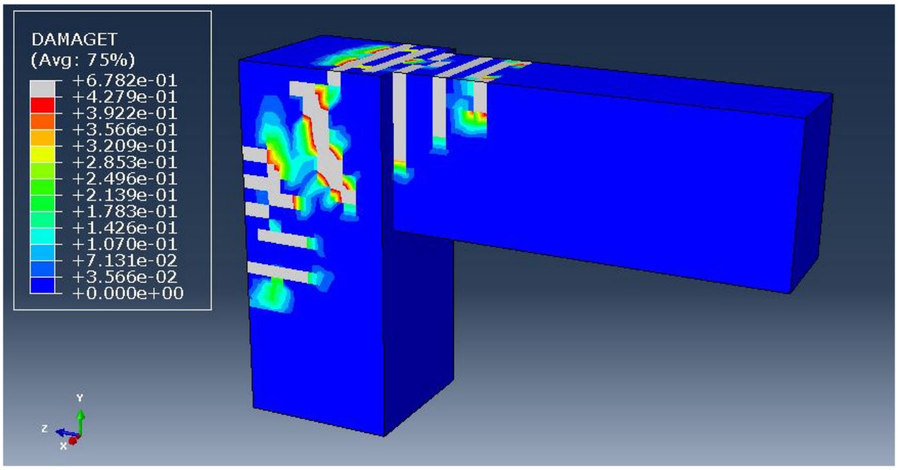

d F6E3 damage in FE model.

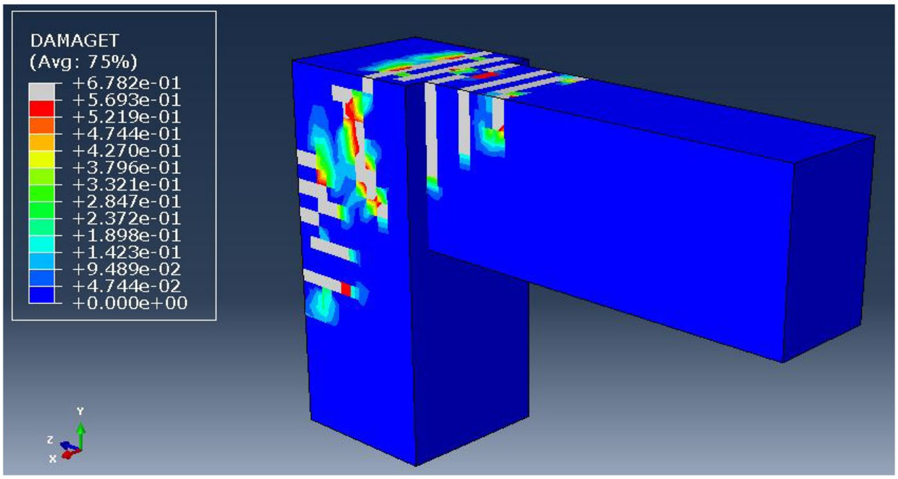

e F6N3 damage in FE model.

Fig. 24 continued

- The reduction in strain imposed on the steel reinforcements indicated significant improvement in overall displacement ductility and toughness under vibrations. Large residual strains were observed on all the HyFRC specimens after yielding steel reinforcements.
- The improved energy dissipation capacity from the fiber-bridging effect significantly contributed to the low rate of stiffness degradation of KJ during the cyclic tests. The Ferro-Ultra hybrid exhibited the best energy dissipation capacity followed by the Ferro-Econo hybrid, Ferro-Super hybrid, Ferro-Nylo hybrid, Ferro-Ferro hybrid and Control.
- As for the KJ's closing action, the average error of margin for all FE models in the peak load capacity, peak load displacement and maximum displacements were in the range of 25.89%, 3.45% and 0.18%, respectively.
- For KJ's opening action, the average error of margin for all FE models in the peak load capacity, peak load displacement and maximum displacements were in the range of 21.27%, 3.79% and 1.28%, correspondingly.

Acknowledgements
The authors would like to thank Innofloor Sdn. Bhd. as the Malaysian FORTA supplier for providing the fibers to conduct this research. Their support is gratefully acknowledged.

Authors' contributions
SMISZ and FH designed the research methodology; SMISZ and FH performed the analysis, SMISZ draft the manuscript; FH reviewed the manuscript; RSMR edited and revised the manuscript. All authors read and approved the final manuscript.

Author's Information
S.M.I.S.Z. is a graduate student at Universiti Putra Malaysia and also a lecturer at Universiti Malaysia Sabah. F.H. and R.S.M.R. is an associate professor at Universiti Putra Malaysia.

Funding
This research was funded by Universiti Putra Malaysia (UPM) under the Putra Grant Research Project, No. 9531200.

Availability of data and materials
The data used to support the findings of this study are available from the authors upon request.

Declarations

Competing interests
The authors declare that they have no competing interests.

Received: 27 July 2020 Accepted: 8 March 2021

References

ACI Committee 318. (2002). Building code requirements for structural concrete (ACI 318–02) and commentary (ACI 318R-02).

ACI Committee 374. (2002). Commentary on Acceptance Criteria for Moment Frames Based on Structural Testing (ACI 374.1–05)," *Am. Concr. Inst. (ACI), Farmingt. Hills, Detroit*, p. 13.

ASTM C39/C39M-16a. (2016). Standard Test Method for Compressive Strength of Cylindrical Concrete Specimens. In *ASTM International*.

Akkaya, Y., Peled, A., & Shah, S. P. (2006). Parameters related to fiber length and processing in cementitious composites. *Materials and Structures, 33*(8), 515–524.

Altoubat, S., Yazdanbakhsh, A., & Rieder, K. A. (2009). Shear behavior of macro-synthetic fiber-reinforced concrete beams without stirrups. *ACI Materials Journal, 106*(4), 381–389.

BS EN 1992–2:2005. (2005). Eurocode 2. Design of concrete structures. Concrete Bridges. Design and detailing rules. *British Standard Institution*.

Angelakos, B. (1999). *The Behaviour of Reinforced Concrete Knee Joints Under Earthquake Loads.* University of Toronto.

Betterman, L. R., Ouyang, C., & Shah, S. P. (1995). Fiber-matrix interaction in microfiber-reinforced mortar. *Advanced Cement Based Materials, 2*(2), 53–61.

Bindhu, K. R., Sukumar, P. M., Jaya, K. P., & Division, S. E. (2009). Performance of exterior beam-column joints under seismic type loading. *ISET Journal of Earthquake Technology, 46*(503), 47–64.

Buratti, N., Mazzotti, C., & Savoia, M. (2011). Post-cracking behaviour of steel and macro-synthetic fibre-reinforced concretes. *Construction and Building Materials, 25*(5), 2713–2722.

Chidambaram, R. S., & Agarwal, P. (2015). Seismic behavior of hybrid fiber reinforced cementitious composite beam-column joints. *Materials and Design, 86,* 771–781.

Chun, S. C., & Shin, Y. S. (2014). Cyclic testing of exterior beam-column joints with varying joint aspect ratio. *ACI Structural Journal, 111*(3), 693–704.

Foroughi-Asl, A., Dimaghani, S., & Famili, H. (2008). Bond strength of reinforcement steel in self-compacting concrete. *International Journal of Civil Engineering, 6*(1), 24–33.

Fu, Q., Niu, D., Zhang, J., Huang, D., & Hong, M. (2018). Impact response of concrete reinforced with hybrid basalt-polypropylene fibers. *Powder Technology, 326,* 411–424.

Guler, S. (2018). The effect of polyamide fibers on the strength and toughness properties of structural lightweight aggregate concrete. *Construction and Building Materials, 173,* 394–402.

Hashim, D. T., Hejazi, F., & Lei, V. Y. (2020). Simplified Constitutive and Damage Plasticity Models for UHPFRC with Different Types of Fiber. *International Journal Concrete of Structured Materials, 14,* 1.

HosseinSaghafi, M., & Shariatmadar, H. (2018). Enhancement of seismic performance of beam-column joint connections using high performance fiber reinforced cementitious composites. *Constructing Building Materials, 180,* 665–680.

Joint ACI-ASCE Committee 352. (2002). Recommendations for Design of Beam-Column Connections in Monolithic Reinforced Concrete Structures.

Kang, T. H. K., Ha, S. S., & Choi, D. U. (2010). Bar pullout tests and seismic tests of small-headed bars in beam-column joints. *ACI Structural Journal, 107*(1), 32–42.

Khanlou, A., MacRae, G., Scott, A., Hicks, S., & Clifton, G. (2012). Shear performance of steel fibre-reinforced concrete. *Australasian Structural Engineering Conference, 1,* 8.

Kheni, D., Scott, R. H., Deb, S. K., & Dutta, A. (2015). Ductility enhancement in beam-column connections using hybrid fiber-reinforced concrete. *ACI Structural Journal, 112*(2), 167–178.

Khose, V. N., Singh, Y., & Lang, D. H. (2012). A comparative study of design base shear for RC buildings in selected seismic design codes. *Earthquake Spectra, 28*(3), 1047–1070.

McCraven, S. C. (2002). Fibers for Tomorrow. *Concrete Construction, 8,* 27–30.

Mo, K. H., Goh, S. H., Alengaram, U. J., Visintin, P., & Jumaat, M. Z. (2017). Mechanical, toughness, bond and durability-related properties of lightweight concrete reinforced with steel fibres. *Materials Structure Construction, 50,* 1.

NA to BS EN 1998–1:2004. (2008). UK National Annex to Eurocode 8. Design of structures for earthquake resistance. General rules, seismic actions and rules for buildings. *British Standard Institution*.

Nakaki, S. D., Englekirk, R. E., & Plaehn, J. L. (2014). Ductile connectors for a precast concrete frame. *PCI Journal, 39*(5), 46–59.

Nayar, S. K., & Gettu, R. (2015). Synergy in toughness by incorporating amorphous metal and steel fibers. *ACI Materials Journal, 112*(6), 821–827.

Parastesh, H., Hajirasouliha, I., & Ramezani, R. (2014). A new ductile moment-resisting connection for precast concrete frames in seismic regions: An experimental investigation. *Engineering Structures, 70,* 144–157.

Sahoo, D. R., Solanki, A., & Kumar, A. (2014). Influence of Steel and Polypropylene Fibers on Flexural Behavior of RC Beams. *Journal of Materials in Civil Engineering, 27*(8), 04014232.

Shen, L., Worrell, E., & Patel, M. K. (2010). Open-loop recycling: A LCA case study of PET bottle-to-fibre recycling. *Resources, Conservation and Recycling, 55*(1), 34–52.

Simulia. (2001). ABAQUS / CAE User ' s Manual. *ABAQUS/CAE User's Man.*, (pp. 1–847)

SivaChidambaram, R., & Agarwal, P. (2018). Performance Evaluation of Metallic and Synthetic Fiber Hybridization on the Cyclic Behavior of Exterior Beam-Column Joint. *Advanced Civil Engineering Materials, 7*(1), 20170137.

Soutsos, M. N., Le, T. T., & Lampropoulos, A. P. (2012). Flexural performance of fibre reinforced concrete made with steel and synthetic fibres. *Construction and Building Materials, 36,* 704–710.

Strezov, I. & Herbertson, J. (2006). A Life Cycle Perspective on Steel Building Materials

Swolfs, Y., Gorbatikh, L., & Verpoest, I. (2014). Fibre hybridisation in polymer composites: A review. *Composition: Part A Application Science Manufacturing, 67,* 181–200.

Teychenne, D. C., & Franklin, R. E. (1997). *Design of normal concrete mixes*. Construction Research Communications Ltd.

Thomas, J., & Ramaswamy, A. (2007). Mechanical Properties of Steel Fiber-Reinforced Concrete. *ASCE, 19,* 385–392.

Tsonos, A. G. (2007). Cyclic Load Behavior of Reinforced Concrete Beam-Column Subassemblages of Modern Structures. *ACI Structural Journal, 104*(4), 468–478.

Wille, K., & Naaman, A. E. (2012). Pullout behavior of high-strength steel fibers embedded in ultra-high-performance concrete. *ACI Materials Journal, 109*(4), 479–488.

Xue, W., & Yang, X. (2010). Seismic tests of precast concrete, moment resisting frames and connections. *PCI Journal, 55*(3), 102–121.

Xue, W., & Yang, X. (2014). Seismic tests of precast concrete, moment-resisting frames and connections. *PCI Journal, 55*(3), 102–121.

Yao, W., et al. (2019). Influence of fiber mixture on impact response of ultra-high-performance hybrid fiber reinforced cementitious composite. *Composite: Part B Engineering, 163,* 487–496.

Yap, S. P., Bu, C. H., Alengaram, U. J., Mo, K. H., & Jumaat, M. Z. (2014). Flexural toughness characteristics of steel-polypropylene hybrid fibre-reinforced oil palm shell concrete. *Materials and Design, 57,* 652–659.

Yin, S., Tuladhar, R., Collister, T., Combe, M., & Sivakugan, N. (2015). Mechanical Properties and Post-crack Behaviours of Recycled PP Fibre Reinforced Concrete. *Concrete, 2015,* 8.

Zainal, S. M. I. S., Hejazi, F., Aziz, F. N. A. A., & Jaafar, M. S. (2020a). Effects of Hybridized Synthetic Fibers on the Shear Properties of Cement Composites. *Materials (Basel), 13*(22), 5055.

Zainal, S. M. I. S., Hejazi, F., Aziz, F. N. A. A., & Jaafar, M. S. (2020b). Constitutive Modeling of New Synthetic Hybrid Fibers Reinforced Concrete from Experimental Testing in Uniaxial Compression and Tension. *Crystals, 10*(10), 885.

Publisher's Note